論文 / 著書情報
Article / Book Information

Title	Centrifuge model tests on large-diameter monopiles in dense sand subjected to two-way lateral cyclic loading in short-term
Authors	Akihiro Takahashi, Naoya Omura, Takaaki Kobayashi, Yukiho Kamata, Satoshi Inagaki
Citation	Soils and Foundations, Vol. 62, Issue 3, 101148
Pub. date	2022, 4

HOSTED BY
ELSEVIER
Available online at www.sciencedirect.com
ScienceDirect
Soils and Foundations 62 (2022) 101148
www.elsevier.com/locate/sandf

Technical Paper

Centrifuge model tests on large-diameter monopiles in dense sand subjected to two-way lateral cyclic loading in short-term

Akihiro Takahashi [a,*], Naoya Omura [b,1], Takaaki Kobayashi [c], Yukiho Kamata [d], Satoshi Inagaki [c]

[a] Department of Civil and Environmental Engineering, Tokyo Institute of Technology, 2-12-1 O-okayama, Tokyo 152-8552, Japan
[b] Nuclear Power Engineering Department, Electric Power Development, Japan
[c] Civil Engineering Design Division, Kajima Corporation, Japan
[d] Tohoku Branch, Kajima Corporation, Japan

Received 15 September 2021; received in revised form 17 March 2022; accepted 22 March 2022

Abstract

To evaluate the lateral resistance of rigid monopiles for wind turbines in dense sand under lateral cyclic loading, centrifuge model tests are performed, focusing on the base resistance and degradation of the soil resistance under two-way lateral cyclic loading in the short-term. The slenderness ratio (embedded pile length to diameter) is varied from 3.75 to 8 and the loading frequency is in the range of 0.002 to 0.4 Hz in the prototype scale. Under cyclic loading with a maximum horizontal displacement of 5% of the pile diameter, the build-up of excess pore water pressure is observed, but the maximum value of the average excess pore water pressure ratio is around 50% in the steady-state for dense sand whose relative density is 80%. A simple analytical model for the rigid piles, considering the base resistance, is derived and then used to quantify the significance of the resistance at the pile base and the degradation of the soil resistance under cyclic loading. When the slenderness ratio is less than 5, a significant contribution of the moment resistance at the base is confirmed. The estimation of the degradation of the horizontal subgrade reaction coefficient using the simple analytical model suggests that, through cyclic shear tests for the determination of the deformation properties of the soil in a laboratory, it is possible to estimate the degradation of the soil stiffness and the parameters for the reduced sway-rocking type of foundation model.

Keywords: Wind turbine foundations; Monopile; Centrifuge modelling; Lateral cyclic loading; Base resistance; Stiffness degradation

1. Introduction

Fixed foundations are the most common type of foundations for offshore wind farms. To reduce the cost of these foundations, the capacity of the turbine increases rapidly (IRENA, 2021). It has been reported that turbines 15 MW in size will be tested for the first time in 2022 and are scheduled for production in 2024 (Hanley, 2021). Given the recent progress, the size of turbines could reach up to 20 MW in a decade or two (IRENA, 2019). To support such giant turbines, the foundation size also has to be large. The most common type of fixed foundations uses monopiles, whose diameter can be over 10 m for a tower supporting these turbines. With such a large diameter, the slenderness ratio (L/D, where L = embedment length of the pile and D = pile diameter) of each monopile

Peer review under responsibility of The Japanese Geotechnical Society.
* Corresponding author.
E-mail addresses: takahashi.a.al@m.titech.ac.jp (A. Takahashi), naoya_omura@jpower.co.jp (N. Omura), t-kobayashi@kajima.com (T. Kobayashi), kamatay@kajima.com (Y. Kamata), inagakis@kajima.com (S. Inagaki).
[1] Formerly: Tokyo Institute of Technology, Japan.

https://doi.org/10.1016/j.sandf.2022.101148
0038-0806/

becomes smaller and the monopile behaves as a semi-rigid or rigid pile. Due to this trend, the behaviour of short piles, i.e., piles with a small slenderness ratio, has been extensively studied and knowledge that contributes to evaluating the performance of short piles has been accumulated.

For short or rigid piles, since the relatively large displacement of the pile base or tip is expected under laterally loaded conditions, the horizontal and rotational resistance at the base, which is negligible in long piles, needs to be considered in the performance evaluation of the foundation. In the analytical studies on short piles in elastic media, solutions based on the analysis of beams in the Winkler type of foundation are available (Hetenyi, 1946; Barber, 1953; Poulos and Davis, 1980; Scott, 1981). These solutions can be used to assess the serviceability limit states, e.g., the limits in the tilt of the foundation, and are used to estimate the natural frequency of the whole wind turbine system. However, they do not consider the horizontal and rotational resistance at the base as their target slenderness ratios are relatively large. Other solutions, based on finite element analyses (Carter and Kulhawy, 1992; Higgins et al., 2013; Kamata and Takahashi, 2021 among the others), consider the existence of the ground below the base, but the contribution of the resistance at the base is not very clear. Shadlou and Bhattacharya (2016), on the other hand, explicitly considered the ground below the base in their dynamic analysis; their study is one of the few that addresses the effect of the ground below the base in the simplified modelling of the foundation stiffness.

Apart from the above analytical studies on elastic grounds, some studies have considered the horizontal and rotational resistance at the base up to the plastic deformation range. Page et al. (2018) modelled a force–displacement relation at the seabed, based on the macro-element approach. Lai et al. (2021) modelled the region below the pivot of the pile using the macro-element approach and combined it with a pile that was laterally supported by $p-y$ springs proposed by Zhang and Andersen (2017). These models are for clayey grounds, but they may have the potential to be extended for use in sandy grounds.

Experiments are essential for the validation of analytical solutions. In the industry-led PISA (Pile–Soil Analysis) Project, large-scale pile loading tests were performed and then evaluated by a three-dimensional finite element analysis and a one-dimensional pile model, supported by several soil-pile interaction springs, including the horizontal and rotational resistance at the base. The tests were performed for a sandy ground at Dunkirk, northern France (McAdam et al., 2020; Taborda et al., 2020). They are of value for the evaluation of the horizontal and rotational resistance at the base, but are limited in terms of monotonic loading. Physical model tests on short piles in sand have also been performed in a laboratory using the geotechnical centrifuge (Choo et al., 2014; Choo and Kim, 2016; Zhu et al., 2016; Baek et al., 2017). These tests were all conducted under drained (or dry) conditions; unfortunately, the resistance at the base was not explicitly considered.

Given the characteristics of offshore wind turbine towers, the effects of vibrations, i.e., cyclic loading, have to be properly considered (DNVGL-ST-0126, 2018; DNVGL-RP-C212, 2019). Monopiles are exposed to cyclic lateral loads due to the rotation of the blades and environmental loads such as wind and waves. Among the many cyclic loading effects, a permanent accumulated tilt of the foundation over the long term is one of the major concerns, and many physical model tests have been performed to examine this tilt (Leblanc et al., 2010; Nanda et al., 2017; Abadie et al., 2019; Xiao et al., 2021; Richards et al., 2021; Rathod et al., 2021 among others). The tests were performed on rigid piles in sand under drained (or dry) conditions. Many of them were one-way cyclic loading tests, as a large accumulation of displacement was expected, while some of them were two-way or multi-directional loading tests.

As for the performance of offshore wind turbine towers during a single storm, normally the most severe storm in the design life, the relevant frequency range in cyclic loading may be determined by the range in wave loading and the natural frequency of the whole wind turbine system. Typically the latter is higher than the former and falls in the range of 0.1 to 1 Hz, depending on the ground conditions and the size of the wind turbine. In this situation, because of the relatively larger loading frequency, partially drained conditions or nearly undrained conditions are expected, i.e., the build-up of excess pore water pressure during cyclic loading. Consequently, degradation of the soil stiffness is expected. Cyclic loading tests on rigid piles with the build-up of excess pore water pressure are rare, with the work by Zhu et al. (2021) being one of the exceptions. However, the loading frequency in their tests covered only that for wave loading (0.0005 to 0.05 Hz).

In this study, to evaluate the lateral resistance of rigid monopiles for wind turbines in dense sand under lateral cyclic loading, physical model tests in a geotechnical centrifuge are performed. This study focuses on the resistance at the pile base and the degradation of the soil resistance under two-way lateral cyclic loading in the short term. Slenderness ratios of $L/D = 3.75$, 5 & 8 are considered for the former, while loading frequencies of $f = 0.002$, 0.2 & 0.4 Hz in the prototype scale are considered for the latter. In the tests with loading frequencies of $f = 0.2$ & 0.4 Hz, as the loading rates are relatively large compared to the hydraulic conductivity of sand, the ground is under partially drained conditions and the build-up of excess pore water pressure during cyclic loading is expected. To quantify the significance of the resistance at the pile base and the degradation of the soil resistance under cyclic loading, a simple analytical model is used for the rigid piles by considering the moment resistance at the pile base.

2. Overview of centrifuge model tests

The centrifuge model tests are carried out on three different models at 50 g using the Tokyo Tech Mark III cen-

trifuge (Takemura et al., 1999). The three tested models in the prototype scale are shown in Fig. 1. All the test conditions and results hereafter are shown in the prototype scale unless otherwise mentioned. Each model monopile is placed near the centre of a rigid box with inner dimensions of 500 × 300 × 360 mm in the model scale (25 × 15 × 18 m in the prototype scale.).

Since the target monopile is a large-diameter pile, tests on piles with a diameter of 5 to 10 m are desirable when considering the possible application of the monopiles to giant turbines planned for the future. Owing to the limitation of the centrifuge used here, however, the pile diameter in the prototype scale had to be reduced. The application of the generalised scaling law (Iai et al., 2005) is one of the choices for accommodating this situation. However, as the application of the generalised scaling law to pile loading tests has not been validated, especially in terms of the incompatibility of the strain in the soil and the structural members, it was decided that the generalized scaling law would not be used in this study. Instead, quarter models are made to be dimensionally similar to the target monopiles, and used as the prototype monopiles, and the ordinary scaling law is applied for the centrifuge modelling. Thus, monopiles with diameters of D = 1.25 & 2 m in the prototype scale are used in this study. The scaling factors for the important parameters are tabulated in Table 1.

The dense sand layer is modelled by Toyoura sand with a relative density of D_r = 80%. The properties of Toyoura sand are tabulated in Table 2. The air pluviation method is used to prepare the model ground. In reality, the piles are usually driven into the ground, whereas the model monopiles are placed inside rigid boxes after making the sand layer below the base of each pile. The sand is then depos-

Table 1
Scaling factors.

Parameter	Prototype/Model
Length	50
Strain	1
Displacement	50
Acceleration	1/50
Time	50
Frequency	1/50
Stress	1
Soil stiffness	1
Bending stiffness of pile	50^4

Table 2
Properties of Toyoura sand.

Parameter	Value
Specific gravity, G_s	2.655
Maximum void ratio, e_{max}	0.916
Minimum void ratio, e_{min}	0.593
Mean diameter, D_{50} (mm)	0.19
D_r = 80%	
Coefficient of permeability, k (m/s)	3.87×10^{-5}
Shear modulus, G_0 (σ'_{m0} = 25 kPa) (MPa)	62.3
Shear modulus, G_0 (σ'_{m0} = 50 kPa) (MPa)	70.4
Shear modulus, G_0 (σ'_{m0} = 100 kPa) (MPa)	95.2
Cyclic shear stress ratio for γ_{DA} = 7.5% in 20 cycles	0.442

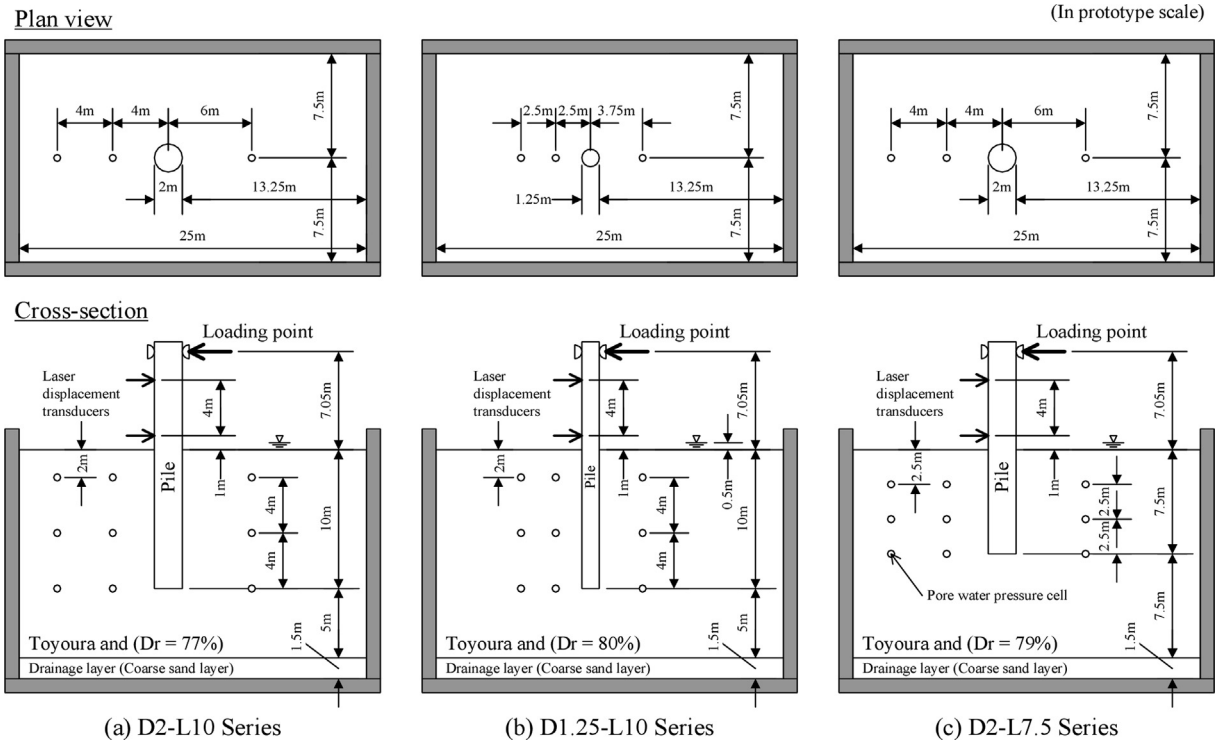

(a) D2-L10 Series (b) D1.25-L10 Series (c) D2-L7.5 Series

Fig. 1. Model configurations in prototype scale.

ited to the designated ground level, i.e., the mudline, in order to avoid the excessive densification of the surrounding soil during the preparation at 1 g. This means that the monopiles in this study are embedded piles. During the preparation of the model ground under dry conditions, pore water pressure cells are placed at the designated locations shown in Fig. 1. Once the preparation of the model ground under dry conditions is completed, the models are saturated with a de-aerated Metolose solution (60 SH-50, hydroxypropyl methylcellulose made by Shin-Etsu Chemical Company) under 760 mm Hg of vacuum pressure. The viscosity of the pore fluid is 50 times that of water, but the density and surface tension are nearly identical to those of water.

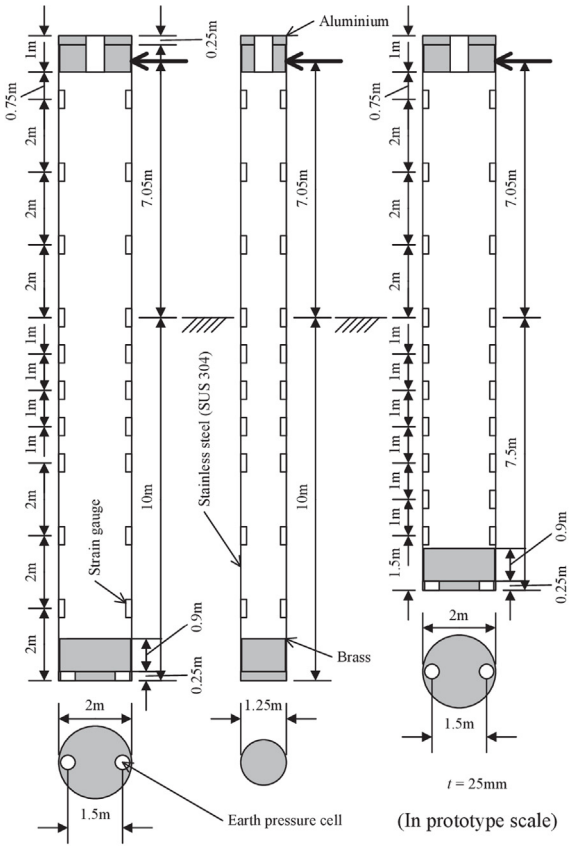

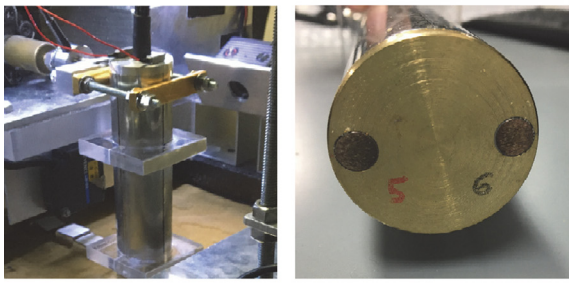

(d) Pile top with clamp

(e) Pile base with pressure cells

Fig. 2. Drawings and photos of model monopiles.

The three model monopiles used in this study are made of stainless steel. They are shown in Fig. 2 and their properties are tabulated in Table 3. Photos of the top and base of model monopile D2-L7.5 are also shown in Fig. 2. Inside the stainless steel tubes, strain gauges are placed at many elevations to estimate the bending moment profile of each monopile. To protect the strain gauges, the base of each monopile is closed with a circular cylinder made of brass so that no soil can enter the pile. In the case of the pile diameter of 2 m, two earth pressure cells are embedded at the bottom of the circular cylinder, as shown in Fig. 2, to estimate the moment resistance at the base. The elevation of the loading height is the same for all the cases (7.05 m) and a hollow circular cylinder made of aluminium is placed at the top of each monopile to prevent local deformation around the loading point.

Two-way lateral loading is created with a hydraulic jack (loading capacity = 7 kN, maximum displacement amplitude = 10 mm, and maximum loading frequency = 20 Hz in the model scale) in the displacement control. To make the bending moment of the pile at the loading point zero, the loading is performed through two half-section brass-made circular cylinders clamping the monopile, as shown in Figs. 1 and 2(d). During the loading, the horizontal displacements of the monopiles are measured at the loading point and at the two elevations shown in Fig. 1 using laser displacement transducers.

The loading tests are performed at 50 g on the three different models shown in Fig. 1. Six loading tests are conducted for each model. The test conditions and some results are tabulated in Table 4. The loading conditions and sequences are summarised in Fig. 3. For all the models, the first three cyclic loadings are performed at a loading frequency of $f = 0.2$ Hz by increasing the loading displacement amplitude in stages, followed by two cyclic loadings at $f = 0.002$ Hz and one cyclic loading at $f = 0.4$ Hz. Since the typical natural frequency of a whole wind turbine system lies in the range of 0.1 to 1 Hz, depending on the ground conditions and the size of the wind turbine, at least it can be said that the loading frequencies of $f = 0.2$ & 0.4 Hz are in the same order as the natural frequency range. As for the displacement amplitude, the displacement amplitude at the loading point lies in the range of 3.2 to 10.3% of the pile diameter. The horizontal displacement at the mudline is around 40 to 50% of that at the loading point; thus, the horizontal displacement amplitude at the mudline is in the range of 1.4 to 4.9% of the pile diameter, which is good enough for performing an assessment in the serviceability limit state.

3. Test results

3.1. Load-displacement curves

Firstly, as typical load–displacement curves, those at the loading point in Model D2-L10 ($D = 2$ m, $L = 10$ m, and $L/D = 5$) with a loading frequency of $f = 0.2$ Hz, are

Table 3
Properties of model monopiles.

	D2		D1.25	
	Model	Prototype	Model	Prototype
Scale factor	1/50	1	1/50	1
Material	SUS 304	SUS 304	SUS 304	SUS 304
Diameter, D (mm)	40	2000	25	1250
Thickness, t (mm)	0.5	25	0.5	25
Area, A (mm^2)	62.0	1.55×10^5	38.5	9.62×10^4
Geometric moment of inertia, I (mm^4)	1.21×10^4	7.56×10^{10}	2.89E $\times 10^3$	1.81×10^{10}
Young's modulus, E (kN/mm^2)	193	193	193	193
Bending stiffness, EI (kN.mm^2)	2.34×10^6	1.46×10^{13}	5.58×10^5	3.48×10^{12}
Loading frequency, f (Hz)	0.1	0.002	0.1	0.002
	10	0.2	10	0.2
	20	0.4	20	0.4

shown in Fig. 4. The results of the three different horizontal displacement amplitude levels are plotted in the figure. With this loading frequency, due to the build-up of excess pore water pressure, the degradation of the soil resistance with the loading cycle occurs and the peak horizontal load at the loading point decreases with the cycle at the beginning of loading, as will be explained later. After around five cycles of loading, the load–displacement curve converges to the same loop and reaches a steady-state for all three cases. These results suggest that degradation of the soil resistance occurs even with a foundation ground that is comprised of dense sand when the monopile is excited at a level of frequency that is the same as that of the natural frequency of the whole wind turbine system.

Similar plots, but for the different loading frequencies in Model D2-L10, are shown in Fig. 5. With the fast loading ($f = 0.2$ & 0.4 Hz, M-2 & F-1), the degradation of the soil resistance with the loading cycle occurs and the curve reaches the steady-state, while the soil resistance increases with the loading cycle with the slow loading ($f = 0.002$ Hz, S-2). The latter is attributed to the densification of the surrounding soil due to the cyclic loading under nearly drained conditions. For the loading with $f = 0.4$ Hz (F-1), it is performed after two slow loadings with $f = 0.002$ Hz (S-2 & S-3), the resistance in the first loading and at the steady-state being larger than that in the loading with $f = 0.2$ Hz (M-2). In all the models, the effects of the densification of the adjacent soil in the slow loading may have a certain impact on the resistance in the loading with $f = 0.4$ Hz, which is performed at the very end of the tests. In Model D2-L10, after all the loadings, the settlement of the ground surface adjacent to the pile is around 300 mm.

Next, typical load–displacement curves for different slenderness ratios with the slow loading ($f = 0.002$ Hz, S-2) are compared in Fig. 6(a) and (b). One shows the plots for the normalised horizontal force at the mudline against the normalised horizontal displacement at the loading point, while the other shows the plots for the normalised moment at the mudline against the normalised horizontal displacement at the loading point. Here, the horizontal force (shear force), H, and the moment, M, at the mudline are estimated from the bending moment distribution estimated by the strain gauges attached to the model monopile. It should be noted that the horizontal force estimated by the strain gauges on the monopile is the same as that measured using a load cell at the loading point (P), while this is not the case for the bending moment. The latter is attributed to the slight shift in the loading point during the cyclic loadings. For this reason, the bending moments estimated by the strain gauges on the monopile are used for the plots and the analysis in the following.

When the horizontal force at the mudline is normalised by the weight of the soil column, whose volume is nearly the same as the pile volume ($\gamma' D^2 L$), the normalised initial stiffness in the first cycle becomes almost the same for all, while the moment at the mudline is normalised by the weight of the same soil column times the embedment length of the pile ($\gamma' D^2 L^2$), and the normalised initial stiffness in the first cycle becomes almost the same for all within the scope of this study. Richards et al. (2021) compared various normalisation methods in order to discuss the effects of the stress level, but no concrete conclusions were obtained. Further comparisons may be needed to justify the normalisation here, but these normalised load–displacement curves allow us to visually grasp the changes in the hysteresis loop depending on the slenderness ratio. When the stored energy at the maximum loading point is W and the area of the load–displacement hysteresis loop, i.e., dissipated energy in one cycle, is ΔW, the hysteresis damping ratio, h, is defined by $h = \frac{1}{4\pi}\frac{\Delta W}{W}$. Detailed comparisons will be made later, but comparisons of the area of these load–displacement loops in the figure reveal that the larger the slenderness ratio, the smaller the hysteresis damping ratio.

Up to now, all the figures have displayed plots against the horizontal displacement at the loading point. However, for a stability assessment of a wind turbine tower, the horizontal displacement and rotation (or tilt) of the monopile at the mudline are needed. Similar plots to those in Fig. 6 are plotted in Fig. 7, but they show the relationships between (a) the horizontal force and the displacement at

Table 4
Test conditions and some results.

Test code	Loading pattern	D (m)	L (m)	D_r (%)	γ' (kN/m^3)	e (m)	f (Hz)	N (-)	δ_{max} (mm)	$\frac{\delta_{max}}{D}$	u_{max} (mm)	$\frac{u_{max}}{D}$	P_1 (MN)	h_H (%)	h_M (%)	n_{h1} (MN/m^3)	$n_{h\min}$ (MN/m^3)	$\frac{n_{h\min}}{n_{h1}}$	r_{uave}	$\eta_1 L$
D2-L10-01	M-1	2	10	77%	9.74	7.05	0.2	20	68	3.4%	36	1.8%	0.28	26%	21%	3.1	1.9	0.61	0.47	1.8
D2-L10-02	M-2	2	10	77%	9.74	7.05	0.2	20	136	6.8%	67	3.4%	0.64	22%	18%	3.3	1.8	0.54	0.50	1.9
D2-L10-03	M-3	2	10	77%	9.74	7.05	0.2	20	203	10.1%	89	4.5%	0.89	19%	15%	3.6	2.1	0.57	0.50	1.9
D2-L10-04	S-2	2	10	77%	9.74	7.05	0.002	3	137	6.8%	55	2.7%	0.55	22%	18%	3.4	3.4	1.00	0.06	1.9
D2-L10-05	S-3	2	10	77%	9.74	7.05	0.002	3	205	10.2%	82	4.1%	0.87	23%	17%	3.6	3.6	1.00	0.08	1.9
D2-L10-06	F-1	2	10	77%	9.74	7.05	0.4	20	81	4.1%	35	1.8%	0.41	24%	18%	4.1	3.0	0.74	0.36	2.0
D1.25-L10-01	M-1	1.25	10	80%	9.79	7.05	0.2	20	40	3.2%	18	1.4%	0.14	16%	7.8%	3.0	2.4	0.79	0.29	2.4
D1.25-L10-02	M-2	1.25	10	80%	9.79	7.05	0.2	20	80	6.4%	39	3.1%	0.30	20%	12%	3.1	1.6	0.50	0.37	2.5
D1.25-L10-03	M-3	1.25	10	80%	9.79	7.05	0.2	20	126	10.1%	62	4.9%	0.39	19%	12%	2.4	1.4	0.57	0.41	2.3
D1.25-L10-04	S-2	1.25	10	80%	9.79	7.05	0.002	3	80	6.4%	35	2.8%	0.23	17%	9.4%	2.2	2.2	1.00	0.04	2.3
D1.25-L10-05	S-3	1.25	10	80%	9.79	7.05	0.002	3	126	10.0%	51	4.1%	0.36	18%	8.9%	2.4	2.4	1.00	0.05	2.3
D1.25-L10-06	F-2	1.25	10	80%	9.79	7.05	0.4	20	83	6.6%	35	2.8%	0.27	20%	11%	2.9	2.2	0.76	0.22	2.4
D2-L7.5-01	M-1	2	7.5	79%	9.77	7.05	0.2	20	69	3.4%	31	1.6%	0.22	22%	26%	4.4*	2.6*	0.60	0.39	1.5
D2-L7.5-02	M-2	2	7.5	79%	9.77	7.05	0.2	20	137	6.8%	62	3.1%	0.40	22%	18%	4.2*	2.1*	0.50	0.36	1.5
D2-L7.5-03	M-3	2	7.5	79%	9.77	7.05	0.2	20	206	10.3%	94	4.7%	0.54	21%	15%	3.9*	1.9*	0.50	0.42	1.4
D2-L7.5-04	S-2	2	7.5	79%	9.77	7.05	0.002	3	137	6.9%	59	2.9%	0.33	25%	23%	3.3*	3.3*	1.00	0.05	1.4
D2-L7.5-05	S-3	2	7.5	79%	9.77	7.05	0.002	3	206	10.3%	89	4.4%	0.50	25%	22%	3.4*	3.4*	1.00	0.07	1.4
D2-L7.5-06	F-1	2	7.5	79%	9.77	7.05	0.4	20	82	4.1%	35	1.8%	0.24	22%	23%	4.6*	3.2*	0.71	0.17	1.5

Note: D = Pile diameter, L = Embedment length, D_r = Initial relative density of sand, $\gamma\prime$ = Effective unit weight of sand, $e = M/H$ = Load eccentricity, f = Frequency of cyclic loading, N = Number of cyclic loadings, δ_{max} = Imposed horizontal displacement amplitude at loading point, u_{max} = Horizontal displacement amplitude at ground surface, P_1 = Horizontal load in first cycle, h_H = Hysteresis damping ratio for $H-u$ curve, h_M = Hysteresis damping ratio for $M-\theta$ curve, n_{h1} = Coefficient of subgrade reaction in first cycle, $n_{h\min}$ = Minimum coefficient of subgrade reaction in cyclic loading, r_{uave} = Average excess pore water pressure ratio, η_1 = Relative stiffness of soil to pile in first cycle.
*Value is estimated with considering moment resistance at pile base with $R_k = k_v/k_h = 4$.

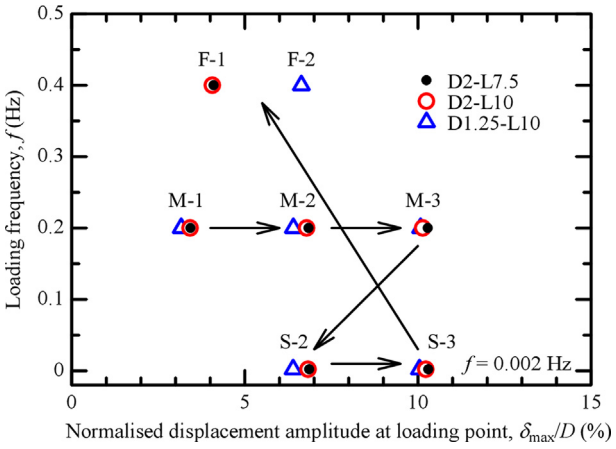

Fig. 3. Loading conditions and sequences.

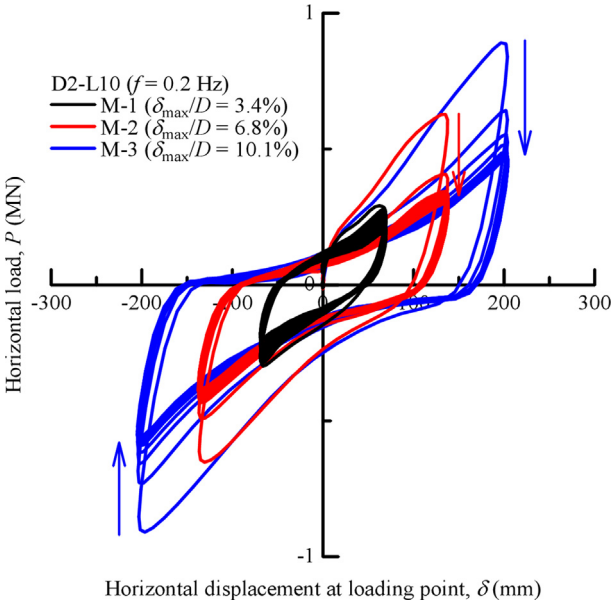

Fig. 4. Load-displacement curves at loading point for different displacement amplitudes (D2-L10).

the mudline and (b) the moment and the rotation at the mudline. A more detailed discussion on the degradation of the soil resistance with the loading cycle will be given later in Section 5 using the secant stiffness, i.e., the slope of the line that passes through the peaks in the loop, in these types of plots. Moreover, the hysteresis damping ratios obtained from these types of plots are compared in the next subsection.

3.2. Hysteresis damping ratios

Changes in the hysteresis damping ratios with the loading cycle are calculated for all the models in all the loadings. The hysteresis damping ratios show some decrease with the loading cycle in the early stage of loading, but reach the steady-state soon after that. The hysteresis damping ratios at the steady-state are summarised in Fig. 8 and

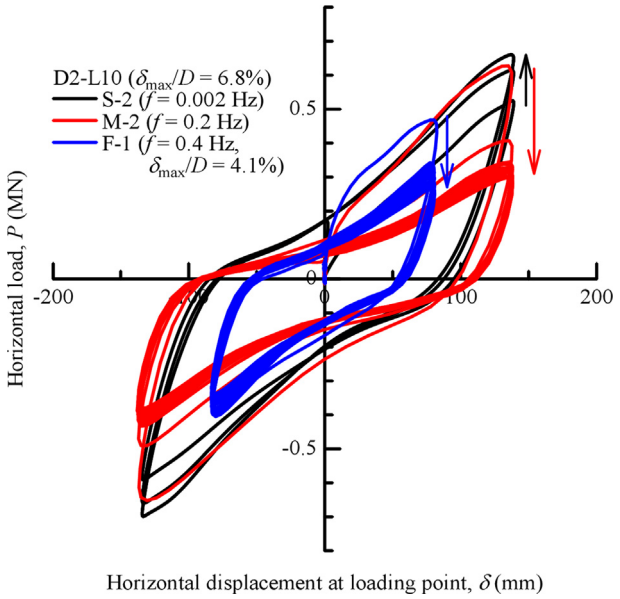

Fig. 5. Load-displacement curves at loading point for different loading frequencies (D2-L10).

Table 4. The average of the last 10 cycles of loading is shown for the cases with 20 cycles, while the average of the three cycles is shown for the slow loadings.

Although some decrease in the damping ratios with the horizontal displacement amplitude at the mudline can be seen for the moment-rotation curves with $D = 2$ m and $f = 0.2$ Hz, the changes in the damping ratios with the displacement amplitude are insignificant as a whole. The condition-dependent difference is less and the damping ratio is around 20% for the horizontal force–displacement curve. On the other hand, the difference depending on the slenderness ratio is significant for the moment-rotation curve; the damping ratio for the case with $L/D = 8$ is around 10%, while it is around 20% for the other cases. Abadie et al. (2019) reported that the damping ratio was around 30% for the cases with $L/D = 4.7$ and $e/L = 1.2$ where e = the load eccentricity at the mudline. Probably the larger load eccentricity in their tests resulted in the larger damping ratio.

In the cases with fast loadings ($f = 0.2$ & 0.4 Hz), because of the significant loading rate effects, e.g., degradation of the soil resistance due to the build-up of the excess pore water pressure and partially drained conditions, comparisons are not easy. Although there are some analytical studies on such effects, e.g., Bayat et al. (2016), further studies may be needed to understand the soil–water coupling effects on the hysteresis damping. If attention is paid only to the cases with slow loading ($f = 0.002$ Hz), the tendency is more simple, namely, the smaller the slenderness ratio, the larger the hysteresis damping ratio, and the difference is significant for the moment-rotation curve.

A possible reason for the above observation is as follows: ordinarily the normalised horizontal displacement with the pile diameter is used as an index for the soil stiff-

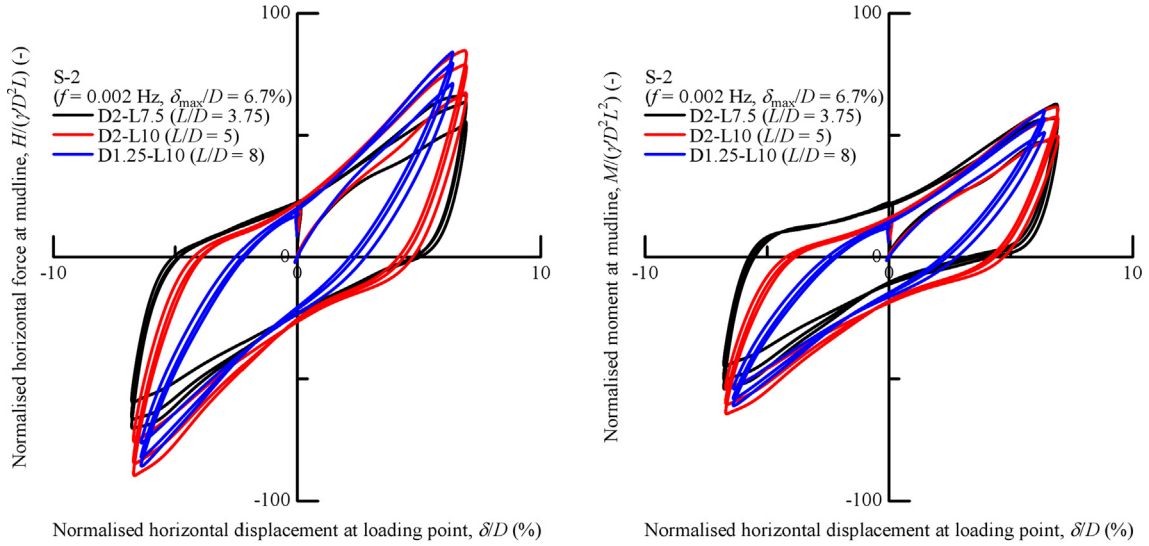

(a) Horizontal force–displacement curves (b) Moment–displacement curves

Fig. 6. Normalised horizontal force and moment at mudline against normalised horizontal displacement at loading point (S-2).

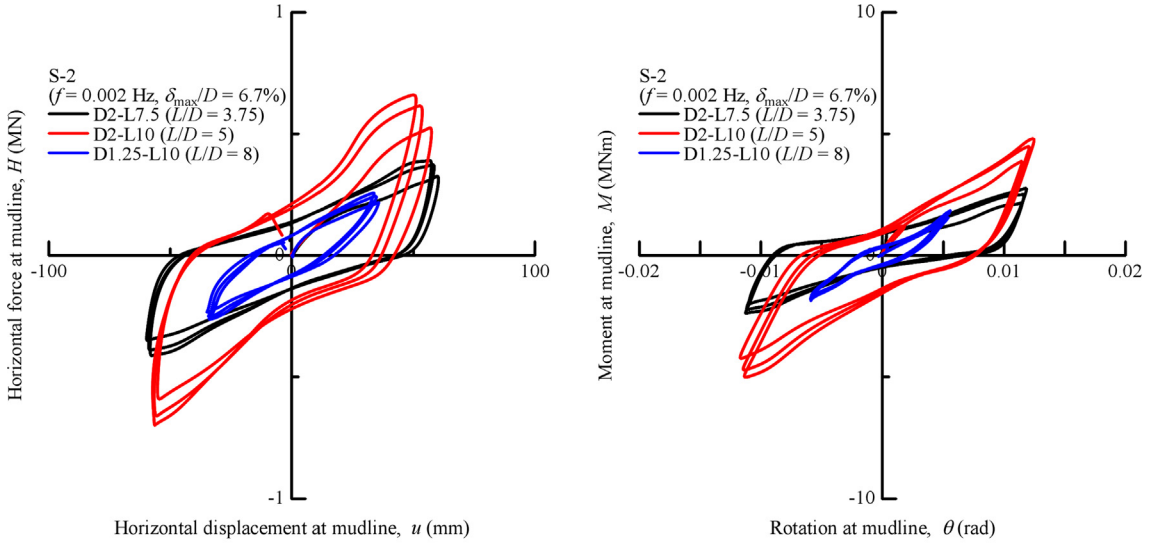

(a) Horizontal force–displacement curves (b) Moment–rotation curves

Fig. 7. Relationships between (a) horizontal force and displacement and (b) moment and rotation at mudline (S-2).

ness since it is believed that the magnitude of the shear strain in a plane normal to the pile axis is directly linked to this index and that it governs the soil stiffness. However, when the pile is rigid, even if the normalised horizontal displacement at the mudline is the same, depending on the pile length, the shear strain in a vertical plane parallel to the loading direction can be different in the deeper portion; if the pile is shorter, larger shear strain is expected in that plane. For this reason, piles with smaller slenderness ratios can experience larger plastic deformation of the soil in the deeper portion; and hence, the hysteresis damping can be larger.

3.3. Excess pore water pressure

With the fast loadings (f = 0.2 & 0.4 Hz), the build-up of excess pore water pressure is observed. Fig. 9 plots the time histories of the excess pore water pressure at depths of $z = 1D$ and $z = 5D$ in Model D2-L10 during M-2 loading (f = 0.2 Hz). In the shallower portion (z = $1D$), the quick build-up of excess pore water pressure is observed in the first cycle, while eight loading cycles are required to reach the steady-state in the deeper portion ($z = 5D$). As expected, the closer the monopile, the larger the excess pore water pressure. Surprisingly, the maximum value in

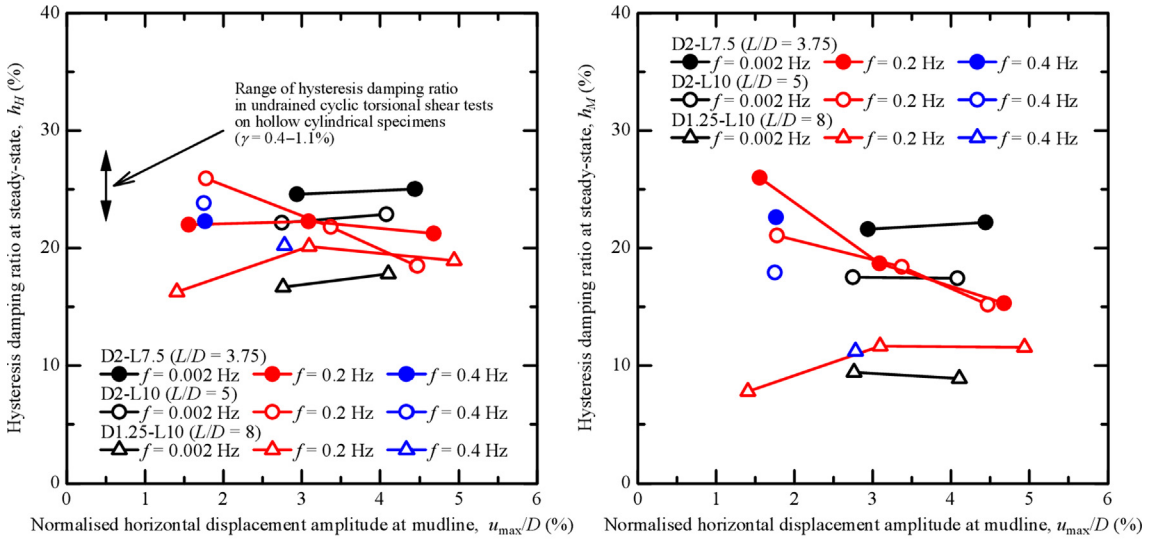

(a) For horizontal force–displacement curves (b) For moment–rotation curves

Fig. 8. Hysteresis damping ratios at steady-state against normalised horizontal displacements at mudline.

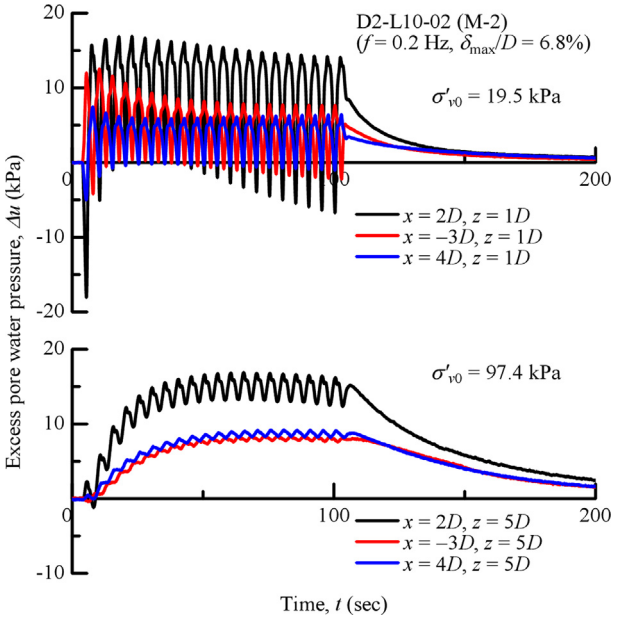

Fig. 9. Time histories of excess pore water pressure (D2-L10-02, M-2).

the deeper portion is more or less the same as that in the shallower portion. This means that the excess pore water pressure ratio r_u (excess pore water pressure Δu normalised by the initial overburden pressure at corresponding point σt_{v0}) is relatively large in the shallower portion, while it is very small in the deeper portion.

As for the dissipation of excess pore water pressure, unlike during an earthquake, since there is no change in the pore water pressure in the far-field, dissipation after loading is rather quick. Some decrease has already started in the shallower portion during cyclic loading because of the partially drained conditions, i.e., the rate of increase in the pore water pressure due to cyclic shearing is not large enough compared to the dissipation rate. Changes in the excess pore water pressure near the monopile ($x = 2D, z = 1D\&5D$) are compared in Fig. 10 for the three different horizontal displacement amplitude levels in the same model (D2-L10). The maximum value per cycle is maintained for the larger displacement amplitude loading (M-3), while some decrease is observed in the smaller displacement amplitude loadings (M-1 & M-2) in the shallower portion. Such tendencies are rather moderate in the deeper portion. In any case, the excess pore water pressure reaches the steady-state in the 10 cycles of cyclic loading in this study.

Fig. 11 plots the maximum excess pore water pressure profiles near the monopile ($x = 2D$) for all the models in all the loadings. In the loading with $f = 0.2$ Hz, there

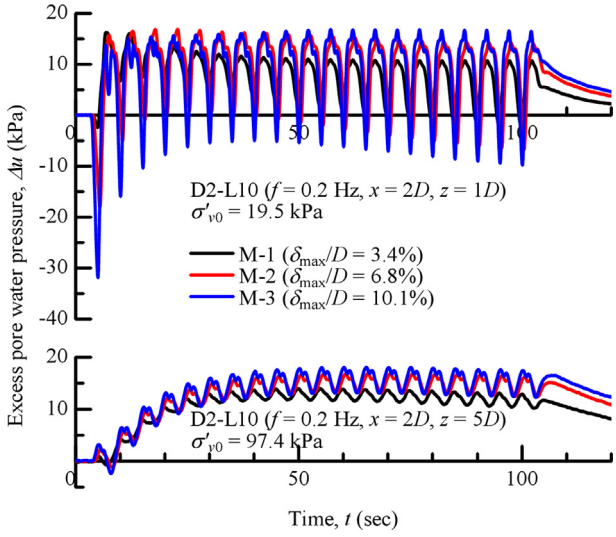

Fig. 10. Time histories of excess pore water pressure near monopile (D2-L10-01 ~ 03, M-1 ~ 3).

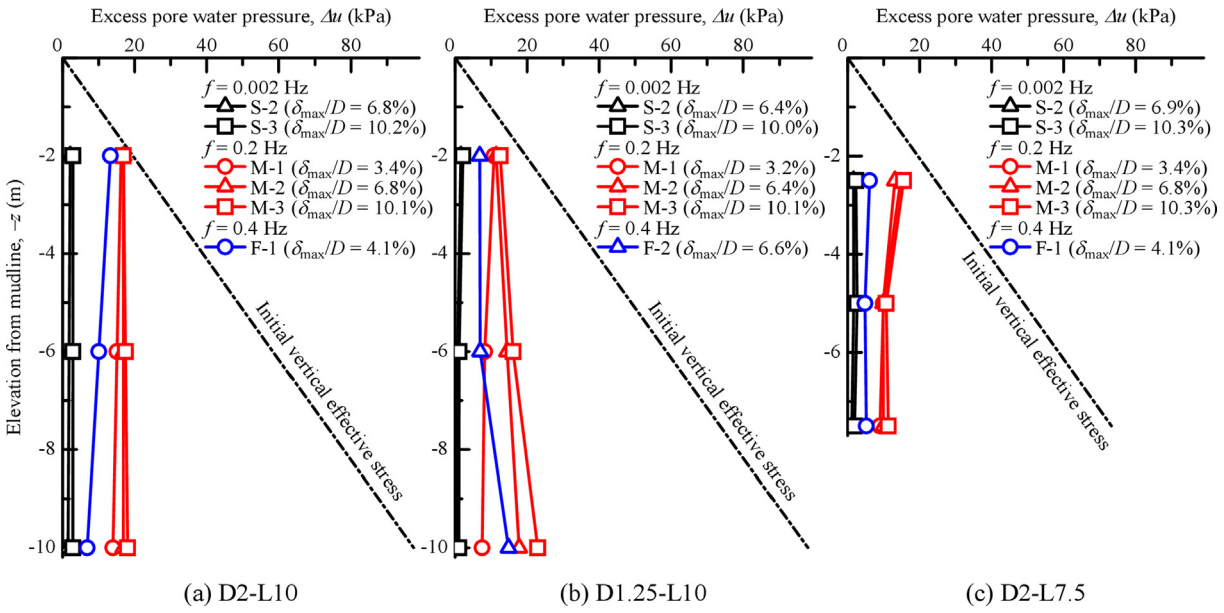

(a) D2-L10 (b) D1.25-L10 (c) D2-L7.5

Fig. 11. Maximum excess pore water pressure profiles near monopile ($x = 2D$).

are some variations, but the values are more or less the same throughout the depth irrespective of the imposed displacement amplitude. In the slow loadings ($f = 0.002$ Hz), there is almost no excess pore water pressure. As for the fastest loadings ($f = 0.4$ Hz), the maximum values are rather smaller even if the loading is the fastest. A possible reason for this is the densification of the adjacent soil in the slow loadings (S-2 & S-3) performed before the loading with $f = 0.4$ Hz, as explained in Fig. 5.

Using the maximum excess pore water pressure profiles, the average excess pore water pressure ratio for the foundation ground, i.e., from the mudline to the monopile base, $r_{u\,\mathrm{ave}}$, is estimated and summarised in Table 4. Even in a dense sand layer, the build-up of excess pore water pressure, i.e., a decrease in effective stress, occurs with cyclic loading. In this study, the maximum horizontal displacement of the monopile at the mudline, normalised by the pile diameter, is around 5%, which is fairly large. However, the soil is far from experiencing liquefaction and the maximum value of the average excess pore water pressure ratio is around 50% within the scope of this study.

3.4. Bending moments

The bending moments of the model monopiles are estimated by the strain gauges attached to them. Comparisons of the bending moment profiles at the peak times in the time histories of the imposed displacement for all the models in all the loadings reveal that the shapes of the bending moment profiles are very similar to each other and show typical bending moment profiles for the free-head rigid or semi-rigid piles.

Fig. 12 plots the bending moment profiles at the selected peaks for all the models in the loadings with the normalised horizontal displacement amplitude of $\delta_{\max}/D = 6.7\%$ at the loading point. The top plots are for the fast loading ($f = 0.2$ Hz, M-2), while the bottom plots are for the slow loading ($f = 0.002$ Hz, S-2). As for the former, since the degradation of the soil resistance occurs during the cyclic loading, the profiles at the first cycle and at the cycle that exhibits the minimum resistance at the peak are shown in the figure. As for the latter, since the peak resistance increases with cycles and three cycles of loading are applied, the profiles at the first and third cycles are plotted. It should be noted that the plots with markers show the bending moments estimated by the strain gauges, while the solid lines indicate the theoretical values that will be explained in Section 4.

In Models D2-L10 and D2-L7.5, the moments at the base estimated by the earth pressure cells are also plotted. They are calculated by assuming that (a) the pressure changes linearly in the loading direction and (b) the pressure is the same if the distance from the neutral axis is the same, i.e., the pressure is the same in the direction normal to the loading direction. Since it is very difficult to measure the earth pressure in a sandy ground, especially with a small cell because of the arching effects, the moment estimated at the base using the earth pressure cell may be underestimated. Unfortunately, this may be the case for the earth pressure measurement in this study.

If a pile is categorised as a long pile, the bending moment converges with zero at the pile tip and the shear force at the tip is expected to be zero if the pile tip is not socketed into the firm layer. None of the piles in this study are long piles, but the bending moment profiles in Model D1.25-L10 show such features. On the other hand, a certain moment resistance seems to be mobilised at the base in the models with the larger diameter piles, especially in Model D2-L7.5, as a larger bending moment is observed near the base of the monopile. As is recommended for

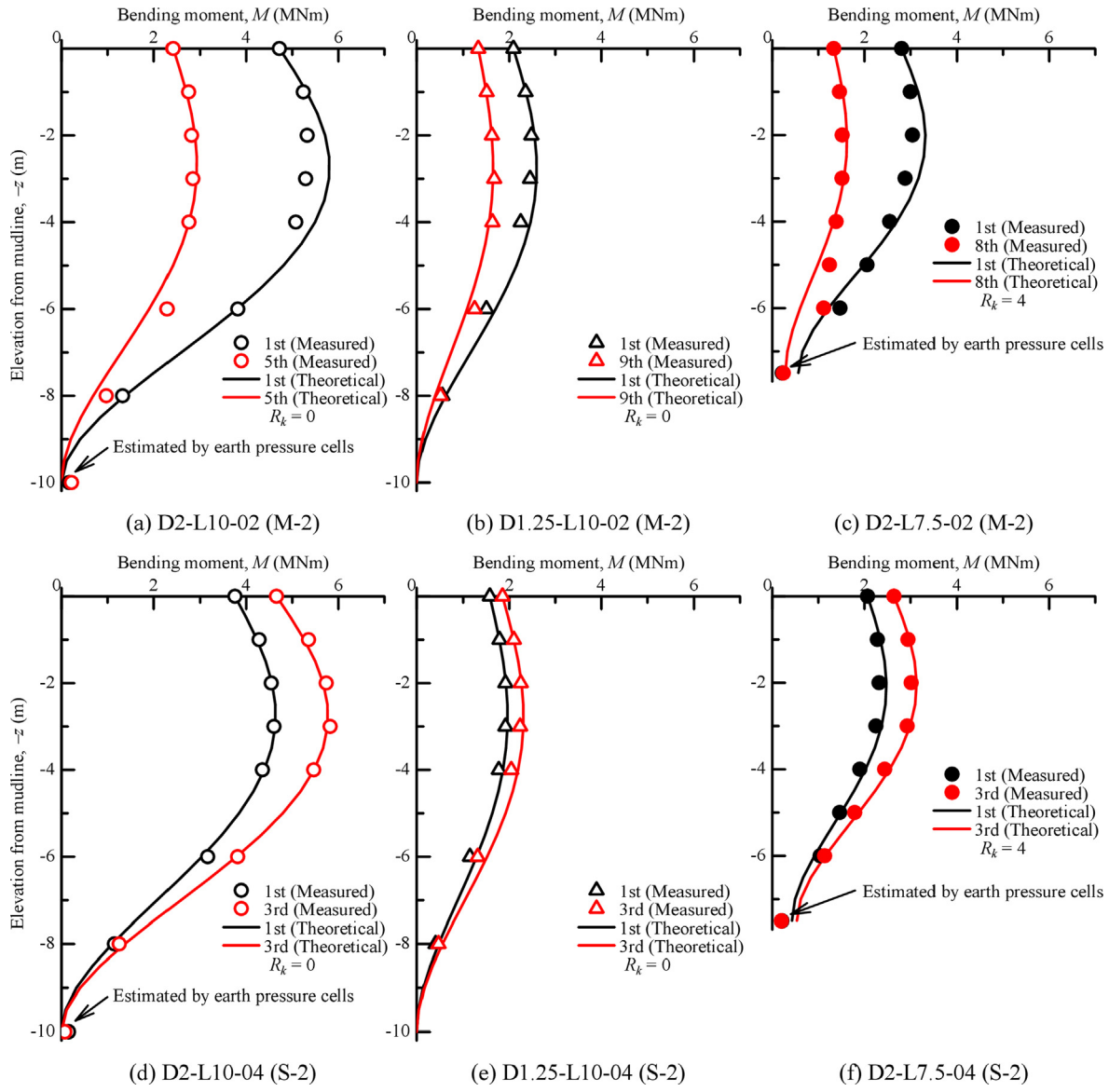

Fig. 12. Maximum bending moment profiles ($\delta_{max}/D = 6.7\%$).

the PISA design model (Burd et al., 2020), consideration of the moment and shear resistance at the base (and distributed moment resistance along the pile) may be needed as they can be significant when the slenderness ratio, L/D, is small. However, the extraction of these components from the experimental results is not easy, since unreliable extrapolation is needed to estimate such resistance at the base. Thus, an attempt is made in the next section to estimate the resistance at the base using a simple model on a rigid pile. That model is also used to estimate the degradation of the soil resistance under cyclic loading.

4. Resistance at base of monopiles

To select an appropriate available analytical solution for the interpretation of the behaviour of piles subjected to lateral load, firstly, distributions of the bending moments in the classic theories and the test results are compared. Fig. 13 compares the bending moment distributions obtained from the theories based on the beam on the elastic Winkler foundation. In the calculations, it is assumed that the length of the pile, $L = 1$, applied horizontal force $H = 1$ and that the load eccentricity at the mudline $e = M/H = 0.7$. These conditions are very similar to those of Model D2-L10 in this study. The moments plotted with markers are for the rigid beam. One is in the foundation ground whose modulus of the subgrade reaction is constant throughout the depth (filled circles), while the other assumes that the modulus increases with depth, i.e., Gibson soil is assumed (open circles). In these solutions, the distribution has nothing to do with the absolute value of the modulus. The solid lines in the figure are obtained by the analytical solution for the finite flexible beam on the Winkler foundation with a constant subgrade reaction modulus

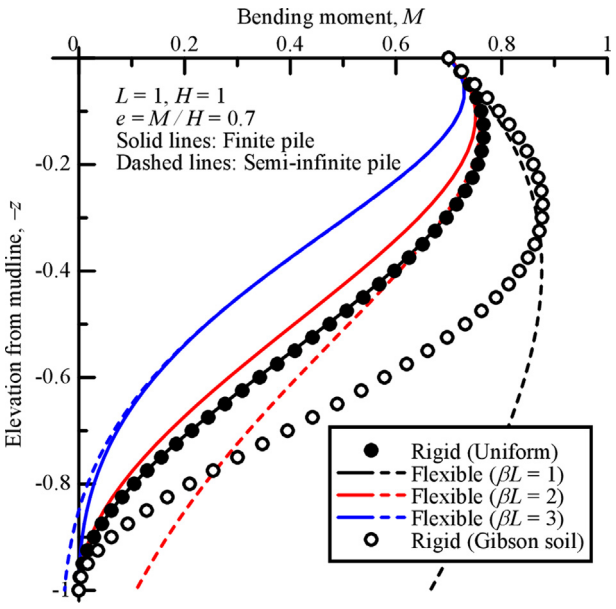

Fig. 13. Bending moment profiles by Winkler foundation models.

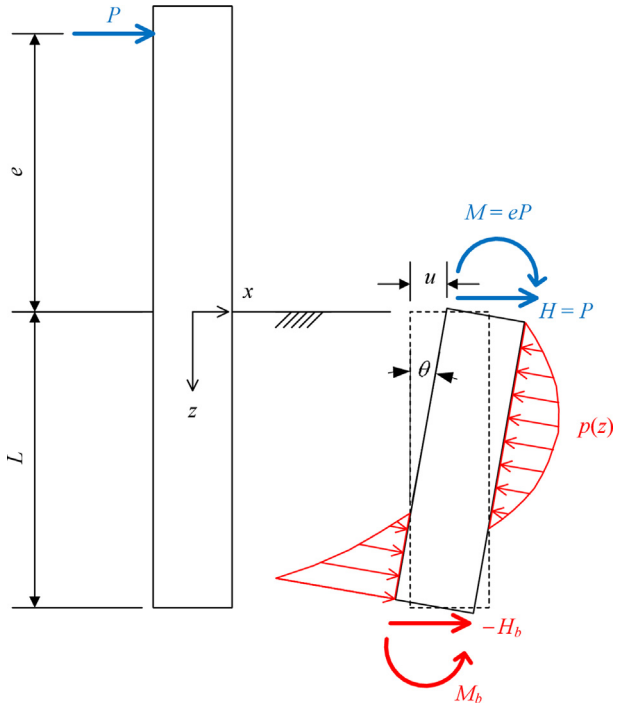

Fig. 14. Rigid pile model used.

throughout the depth. Depending on the parameter for the relative stiffness of the foundation ground to the beam, $\beta = \sqrt[4]{k_h D/4EI}$, where k_h is the modulus of subgrade reaction, the shape of the bending moment distribution changes. The distribution is almost the same as that for the rigid beam with the uniform subgrade reaction modulus when $\beta L = 1$, and even for $\beta L = 2$, the distribution is closer to the rigid beam solution. This suggests that the moment distribution for the semi-rigid pile can be modelled as that for a rigid pile. The dashed lines in the figure are obtained by the analytical solution for the semi-infinite flexible beam. The distribution is almost the same as that for the finite flexible beam when $\beta L = 3$, while it is largely different from the finite flexible beam when βL is small.

If these are compared with the actual bending moments obtained in the tests in Fig. 12, it is obvious that the solutions for the rigid pile in the Gibson soil (plotted with open circles) are very close to those of the observation. Thus, in the following, the solutions based on considering the soil resistance at the base are derived by referring to Hetenyi (1946), Barber (1953), Poulos & Davis (1980), and Scott (1981) and are compared to the observation to quantify the soil resistance at the base. The target situation is illustrated in Fig. 14. It is assumed that the modulus of subgrade reaction is proportional to the depth from the mudline, $k_h(z) = n_h z/D$, where n_h = coefficient of horizontal subgrade reaction. The moment and shear resistance at the base are assumed to be expressed as

$$M_b = K_r\theta = \left(\alpha_r n_h L^4\right)\theta \tag{1}$$

$$H_b = K_s x(L) = \left(\alpha_s n_h L^2\right)x(L) \tag{2}$$

where $x(L)$ is the horizontal displacement at the base ($z = L$), and α_r and α_s are constants.

By satisfying the equilibrium condition in the direction normal to the pile axis and the equilibrium of moments around a certain point in the pile, for instance, around the base of the pile, the horizontal displacement of the pile at a depth of z, $x(z)$, when the pile is subjected to horizontal force H and moment M at the mudline level, can be derived as

$$x(z) = -\frac{24(1+3\alpha_s)H}{(1+36\alpha_r+6\alpha_s+72\alpha_r\alpha_s)n_hL^3}\left\{z-\frac{3(1+4\alpha_r+4\alpha_s)}{4(1+3\alpha_s)}L\right\} - \frac{36(1+2\alpha_s)M}{(1+36\alpha_r+6\alpha_s+72\alpha_r\alpha_s)n_hL^4}\left\{z-\frac{2(1+3\alpha_s)}{3(1+2\alpha_s)}L\right\}. \tag{3}$$

The details of the derivation of Eqn. (3) are provided in Appendix A. By using this equation, the relationship between the forces acting at the mudline (H, M) and the displacement and the rotation at the mudline (u, θ) can be obtained as follows:

$$\begin{pmatrix} H \\ M \end{pmatrix} = \begin{bmatrix} K_L & K_{LR} \\ K_{RL} & K_R \end{bmatrix}\begin{pmatrix} u \\ \theta \end{pmatrix} = \begin{bmatrix} \left(\frac{1}{2}+\alpha_s\right)n_hL^2 & -\left(\frac{1}{3}+\alpha_s\right)n_hL^3 \\ -\left(\frac{1}{3}+\alpha_s\right)n_hL^3 & \left(\frac{1}{4}+\alpha_r+\alpha_s\right)n_hL^4 \end{bmatrix}\begin{pmatrix} u \\ \theta \end{pmatrix} \tag{4}$$

where $u = x(0)$ and $\theta = -\frac{dx(0)}{dz}$.

The horizontal soil reaction, $p(z)$, can be determined by $p(z) = k_h D x(z) = (n_h z)x(z)$. By double integrating this with appropriate boundary conditions, the moment distribution can be obtained as follows:

$$M(z) = HL\left\{\left(\frac{z}{L}\right) - \frac{3(1+4\alpha_r+4\alpha_s)}{1+36\alpha_r+6\alpha_s+72\alpha_r\alpha_s}\left(\frac{z}{L}\right)^3 + \frac{2(1+3\alpha_s)}{1+36\alpha_r+6\alpha_s+72\alpha_r\alpha_s}\left(\frac{z}{L}\right)^4\right\} + M\left\{1 - \frac{4(1+3\alpha_s)}{1+36\alpha_r+6\alpha_s+72\alpha_r\alpha_s}\left(\frac{z}{L}\right)^3 + \frac{3(1+2\alpha_s)}{1+36\alpha_r+6\alpha_s+72\alpha_r\alpha_s}\left(\frac{z}{L}\right)^4\right\}. \quad (5)$$

Fig. 15 plots the changes in the moment profiles with the resistance at the base. In Fig. 15(a), only the moment resistance at the base is considered, i.e., $\alpha_s = 0$ and $\alpha_r > 0$, while only the shear resistance is considered in Fig. 15(b), i.e., $\alpha_r = 0$ and $\alpha_s > 0$. For the former, $\frac{dM(L)}{dz} = 0$ and M_b increases with α_r. For the latter, $M(L) = 0$ and $(-H_b) = -\frac{dM(L)}{dz}$ increases with α_s. If they are compared with the observations shown in Fig. 12, the contributions of M_b and H_b do not look significant for Models M2-L10 and M1.25-L10. However, for Model M2-L7.5, if the base moments estimated by the earth pressure cells are ignored because of their low reliability, the contribution of M_b looks more significant. Thus, in the following, the contribution of the moments at the base is estimated by comparing the solution with the test results without considering the shear resistance at the base ($\alpha_s = 0$).

If it is assumed that the monopile base acts as a rigid foundation on the Winkler foundation, vertical stiffness, K_v, and rotational stiffness, K_r, can be expressed as

$$K_v = \frac{\pi k_v D^2}{4} \quad K_r = \frac{\pi k_v D^4}{64} \quad (6)$$

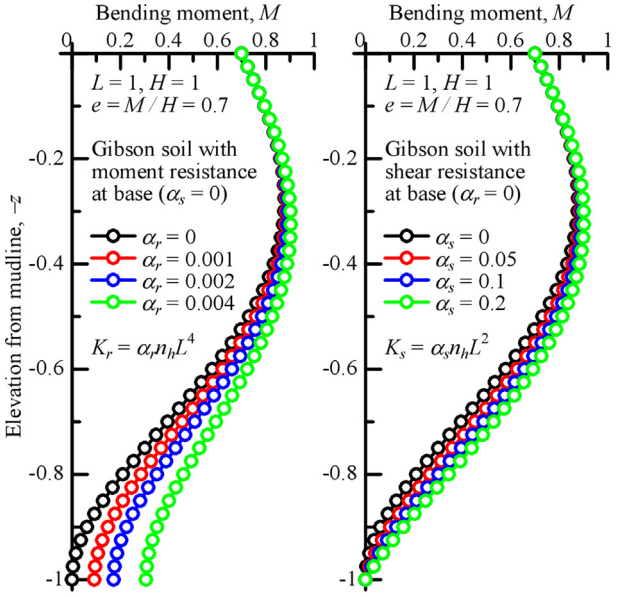

(a) M_b only ($H_b = 0$) (b) H_b only ($M_b = 0$)

Fig. 15. Changes in bending moment profile with base resistance.

by using the modulus of vertical subgrade reaction, k_v. If it is assumed that $k_v = R_k k_h(L) = R_k n_h L/D$, by introducing the ratio of the vertical subgrade reaction modulus to the horizontal one, R_k, α_r in the above solution is expressed as follows:

$$K_r = \alpha_r n_h L^4 = \frac{\pi R_k n_h L D^3}{64} = \frac{\pi}{64} R_k \left(\frac{D}{L}\right)^3 n_h L^4$$

$$\alpha_r = \frac{\pi}{64} R_k \left(\frac{D}{L}\right)^3 \quad (7)$$

A solution with a constant subgrade reaction modulus is given in Appendix B.

Now, the contribution of the moment resistance at the base is estimated by comparing the solution with the observation. Since Model D2-L7.5 has the smallest slenderness ratio and the contribution of the moment resistance at the base is expected to be significant, comparisons are firstly made for this model. The bending moment distributions at the peak in the first cycle for the slow loadings (S-2 & S-3) are plotted in Fig. 16 together with the solutions with the different R_k. If the base moments estimated by the earth pressure cells are ignored because of their low reliability, $R_k = 4$ provides the best fits. This means that the vertical subgrade reaction modulus is four times the horizontal one, which looks too large. This is probably due to the use of the Winkler foundation model for the vertical reaction. Since there is no interaction between the adjacent springs in the Winkler model, it is said that the rotational stiffness becomes too soft (Houlsby et al., 2005). If the solution for a rigid circular foundation on an elastic halfspace is used (Poulos and Davis, 1974), $K_v = 2GD/(1-\nu)$ and $K_r = GD^3/3(1-\nu)$, i.e.,

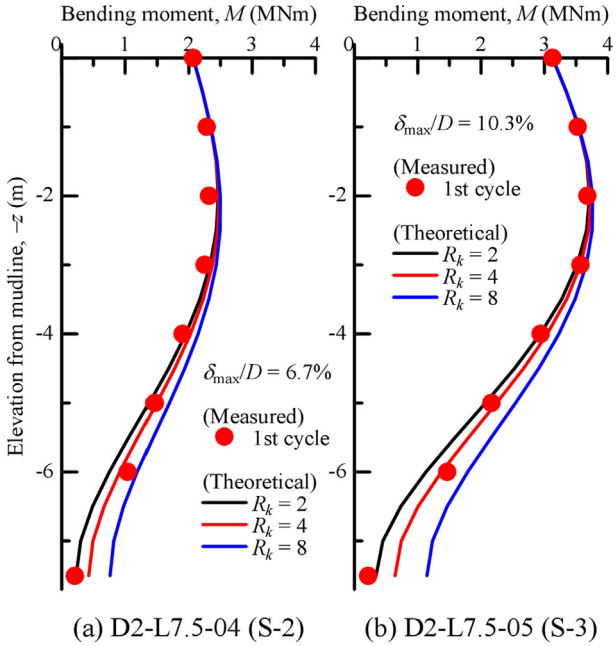

(a) D2-L7.5-04 (S-2) (b) D2-L7.5-05 (S-3)

Fig. 16. Comparisons of measured and theoretical maximum bending moment profiles ($f = 0.002$ Hz).

$K_r/K_v = D^2/6$, while $K_r/K_v = D^2/16$ for the Winkler foundation. This means that a larger vertical subgrade reaction is needed to have proper rotational resistance in the Winkler model. Considering this situation, $R_k = 4$ corresponds to the ratio of the vertical soil stiffness to the horizontal one in the elastic halfspace of $4 \times 6/16 = 1.5$, which is quite reasonable. The same estimation has been done for Models D2-L10 and D1.25-L10, and it reveals that $R_k = 0$ is reasonable for these models. This indicates that significant moment resistance at the base can be expected when slenderness ratio L/D is less than five.

The theoretical solutions shown in Fig. 12 are plotted with $R_k = 0$ for Models D2-L10 and D1.25-L10, and with $R_k = 4$ for Model D2-7.5. It can be said that the observed and theoretical solutions are comparable, which indicates that (a) the assumption of Gibson soil is reasonable even for the cases with the build-up of excess pore water pressure during cyclic loading and (b) it is possible to explain the base resistance as the rotational resistance and to quantify its contribution by using the simple model within the scope of this study. The implication of the former is that, in the tests with the build-up of excess pore water pressure during cyclic loading, the distribution of the effective stress is not proportional to the depth, as shown in Fig. 11, i.e., the soil stiffness is not proportional to the depth in a strict sense. However, Gibson soil is still applicable when the build-up of the excess pore water pressure is not too large. The implication of the latter is that, with or without consideration given to the moment resistance at the base, the horizontal displacement at the mudline can change by 13% under the same applied load for Model D2-L7.5.

5. Stiffness degradation under cyclic loading

By using the simple model derived in the previous section, the degradation of the soil stiffness under cyclic loading is evaluated. To examine the degradation, the initial stiffness is important. However, the loading test starts with the relatively fast loading ($f = 0.2$ Hz) and the build-up of the excess pore water pressure is significant from the first cycle. Thus, to evaluate the initial stiffness, the very beginning of the first slow loading ($f = 0.002$ Hz, S-2), after the three fast loadings, is used. Fig. 17 plots the relationships between (a) the horizontal force and the displacement and (b) the moment and the rotation at the mudline at the small displacement level (S-2). The data points are scattered, but for the horizontal force–displacement curves up to 0.2% of the pile diameter displacement (4 mm for Models D2-L10 & D2-L7.5 and 2.5 mm for Model D1.25-L10), the monopiles show nearly linear responses. Thus, the values for the coefficient of horizontal subgrade reaction, n_h, in this range, are estimated by Eqn. (4) with keeping the parameter for base resistance, R_k, constant ($R_k = 0$ for Models D2-L10 and D1.25-L10 and $R_k = 4$ for Model D2-7.5). Since the load eccentricity at the mudline ($e = M/H$) is constant, it is possible to write Eqn. (4) as

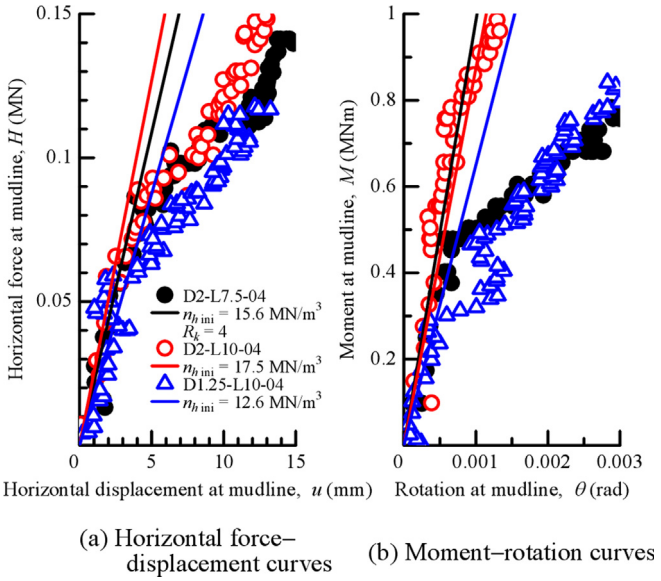

Fig. 17. Horizontal force and displacement and moment and rotation at mudline in small displacement level (S-2).

a single equation that relates H and u. In doing so, however, there is a perfect match for the horizontal response, but not for the rotational response. Thus, the coefficient is estimated by minimising the norm, $\sqrt{\delta u^2 + (D\delta\theta)^2}$, for the given H and M. The results are shown as solid lines in Fig. 17. In the following, these values are treated as the initial values of the coefficient of horizontal subgrade reaction, $n_{h\,\mathrm{ini}}$.

To examine the degradation of the soil stiffness, by choosing the responses of the monopiles at the peak times in the time histories of the imposed displacement for all the models in all the loadings, the variation in the coefficient of horizontal subgrade reaction, n_h, with the cycle is estimated by Eqn. (4) with keeping the parameter for base resistance, R_k, constant as with the initial stiffness evaluation. The values estimated here correspond to a kind of secant stiffness, i.e., the slope of the line that passes through the peaks in the hysteresis loop. All the results are shown in Fig. 18 together with the plots normalised by the coefficient in the first loading cycle and those normalised by the initial stiffness in the small displacement level. The values in the first cycle and in the cycle that exhibits the minimum resistance during loading are also summarised in Table 4. Since the rigid beam on the Winkler foundation is applicable when the relative stiffness of the soil to the pile, $\eta = \sqrt[5]{n_h/EI}$, satisfies $\eta L < 2$ (Poulos and Davis, 1980), the index for the first cycle, $\eta_1 L$, is also tabulated in Table 4. This criterion is almost satisfied for Models D2-L10 and D2-L7.5 ($L/D = 5$ & 3.75), but is slightly exceeded for Model D1.25-L10 ($L/D = 8$). Probably for this reason, the value of n_h for Model D1.25-L10 is smaller than that for the other models.

The values of n_h in this study are compared to those in the literature. Terzaghi (1955) suggested $n_h = 11$, 4.4 &

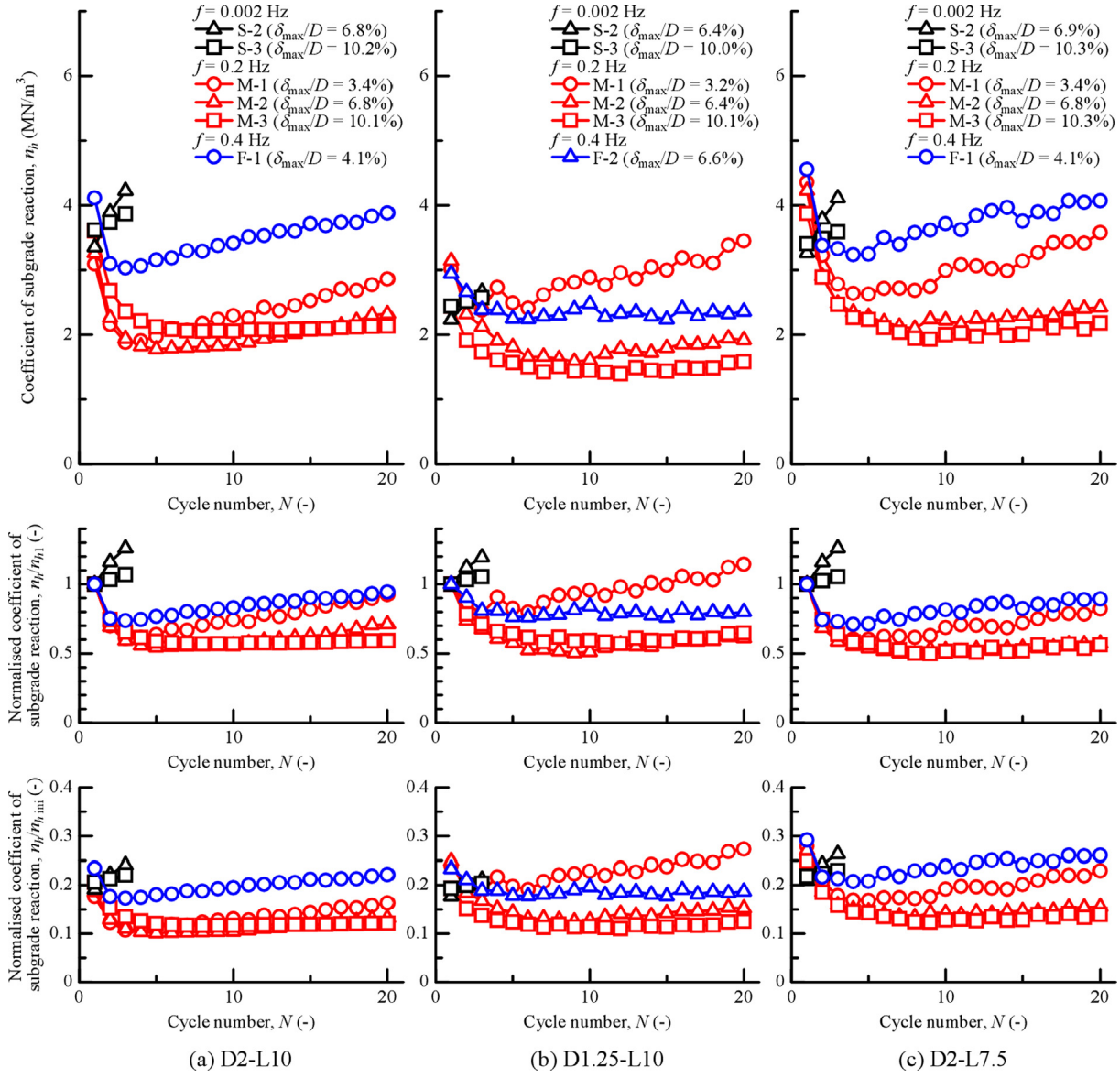

Fig. 18. Changes in coefficient of subgrade reaction, n_h, during cyclic loading.

1.3 MN/m^3 for dense, medium, and loose submerged sands, respectively, as typical values. Elson (1984) suggested that Terzaghi's values should be used as lower limits and proposed the upper limit as a function of the relative density of sand, which gives n_h = 30 MN/m^3 for D_r = 80%. Davisson (1970) suggested n_h = 2.7 to 27 MN/m^3 for granular soils. The strain levels are unknown, but they fall in a range of those obtained in this study. Bhushan et al. (1981) conducted tests on drilled and cast-in-place piers with D = 0.61–1.22 m and L = 5.18–5.49 m, and made a chart to estimate n_h by considering the density and normalised displacement at the ground surface. According to the formula proposed by Zhang (2009), referring to the work by Bhushan et al. (1981), n_h = 20 MN/m^3 for $x(0)/D$ = 1.5% and n_h = 11 MN/m^3 for $x(0)/D$ = 5% in submerged sand with D_r = 80%. For the estimation of these values, the initial portion of the $p-y$ curve adopted in the API specifications (API, 2000) was used, which yields a three-to-four-fold coefficient, but is not far from the value estimated by the loading tests. The estimated values for n_h are somewhat smaller than the above-mentioned values, but this is not so surprising as the monopiles are embedded piles in this study.

The stiffness decreases with the number of cycles and reaches the steady-state in the loadings with the relatively large build-up of excess pore water pressure (M-2 & M-3). In these cases, the stiffness becomes half of that in the first cycle and is around 10 to 15% of the initial stiffness estimated in the small displacement level. On the other hand, in the fast loading, but with the smaller displacement amplitude (M-1), and the fast loading on the ground densified by the previous slow loadings under nearly drained conditions (F-1 or F-2), some increase in stiffness is observed after the significant decrease in stiffness in the early stage of loading. The former is attributed to some densification with the continuous dissipation of the gener-

ated excess pore water pressure during cyclic loading, while the latter may be due to the dilation of the densified sand in the previous cyclic loadings.

Fig. 19 plots the minimum coefficient of the horizontal subgrade reaction normalised by the coefficient in the first cycle, $n_{h\,\min}/n_{h1}$, against the average effective stress ratio, $1 - r_{u\,\mathrm{ave}}$. Here, $r_{u\,\mathrm{ave}}$ is the average excess pore water pressure ratio in the foundation ground. The numeric data are also found in Table 4. The plot for $n_{h\,\min}/n_{h1}$ against $(1 - r_{u\,\mathrm{ave}})$ shows the one-to-one relationship. This suggests

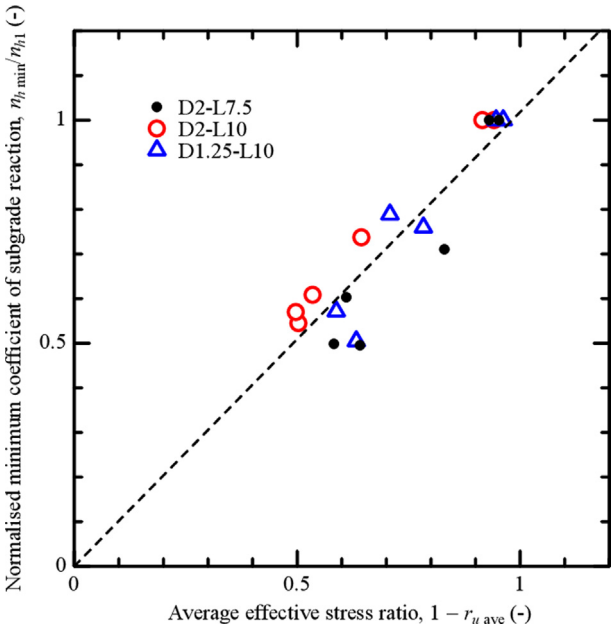

Fig. 19. Normalised minimum coefficient of subgrade reaction against average effective stress ratio.

that, if the average pore water pressure ratio for the foundation ground and the resistance in the first loading can be estimated, it is also possible to estimate the soil stiffness degradation for the steady-state. However, this is not very useful as it is the estimation of the resistance in the first loading that is needed.

A comparison is also made here with the cyclic shear tests performed in the laboratory to examine the similarity in the decay of stiffness with straining. The soil stiffness estimated by loading tests, $n_{h\,\min}z_{25}$, and that estimated by undrained cyclic torsional shear tests on hollow cylindrical specimens, $2(1+\upsilon)G$, are plotted against the estimated pile-loading-induced equivalent shear strain in the ground or shear strain in Fig. 20. Here, $0.6u_{\max}/D$ is the pile-loading-induced equivalent shear strain estimated by referring to the works by Blaney and O'Neill (1986) and Kagawa and Kraft (1980) using the normalised horizontal displacement amplitude at the mudline, $u_{\max}/D$. The cyclic shear tests are on Toyoura sand with a relative density of 80%. Here, z_{25} is a depth at $\sigma\prime_{v0} = 25$ kPa, i.e., $n_{h\,\min}z_{25}$ corresponds to the soil stiffness at a confining pressure of 25 kPa, G is the shear modulus, υ is Poisson's ratio, and $2(1+\upsilon)G$ corresponds to the Young's modulus of the soil. In the plots, $\upsilon = 0.5$ is assumed. The markers at $0.6u_{\max}/D = 0.6 \times 0.2\% = 0.12\%$ correspond to the initial stiffness in the small displacement level in Fig. 17 and the lines are obtained by the shear tests under $\sigma\prime_{m0} = 25$, 50 & 100 kPa. The markers obtained by the pile loading tests are well above and not on the line obtained by the cyclic shear tests under $\sigma\prime_{m0} = 25$ kPa, but their trends in stiffness decay with shearing are very similar. There are several reasons for the discrepancy, namely, (a) the estimated pile-loading-induced equivalent shear strain in the ground,

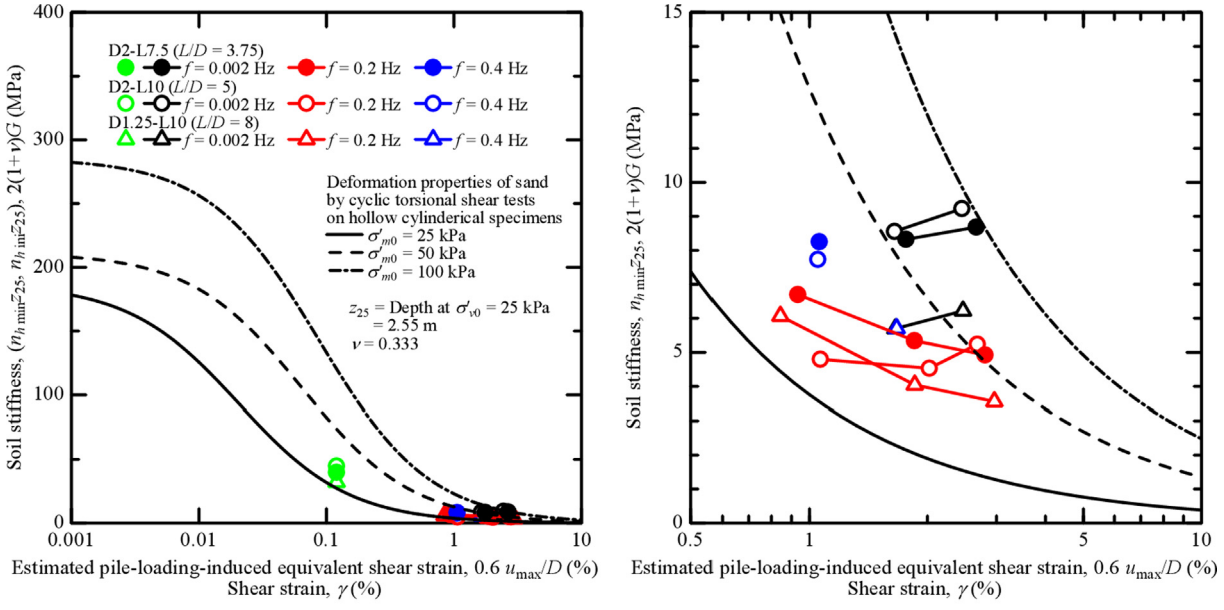

Fig. 20. Soil stiffness estimated by loading tests and that by undrained cyclic torsional shear tests.

$0.6u_{max}/D$, does not have to be the shear strain of the relevant soil mass in this study, (b) partial drainage takes place during the cyclic loading, making the stiffness larger, and (c) the differences in the shearing modes and anisotropy of the soil result in the different values for the modulus. It is also worth noting that the stiffness for the slow loading ($f = 0.002$) is larger than the stiffness for the fast loadings ($f = 0.2$ & 0.4 Hz). This is attributed to the almost non existent excess pore water pressure during the slow cyclic loading. Since the shear tests presented here are performed under undrained conditions, this difference should be considered in the determination of the soil stiffness when the slow loading is of interest. It is impossible to obtain a very useful quantitative conclusion only from the tests shown here, but at least it can be said that, through cyclic shear tests for the determination of the deformation properties of soil in a laboratory, it is possible to estimate the degradation of the soil stiffness and parameters for the reduced sway-rocking type of foundation model like Eqn. (4) for dense sand, as for clay (Zhang and Andersen, 2017) and carbonate soils (Erbrich et al., 2011).

6. Conclusions

To evaluate the lateral resistance of rigid monopiles for wind turbines in dense sand under lateral cyclic loading, centrifuge model tests were performed, focusing on the base resistance and degradation of the soil resistance under two-way lateral cyclic loading in the short-term. The slenderness ratio, defined as the embedment pile length to the diameter, L/D, was varied from 3.75 to 8, the loading frequency, f, was in the range of 0.002 Hz to 0.4 Hz in the prototype scale, and the build-up of the excess pore water pressure was observed in the fast loadings. A simple analytical model for rigid piles, considering the base resistance, was derived and used to quantify the significance of the resistance at the pile base and the degradation of the soil resistance under cyclic loading. The major findings obtained in this study are as follows:

- Degradation of the soil resistance occurs even in a foundation ground that is comprised of dense sand when the monopile is excited at a level of frequency that is the same as that of the natural frequency of the whole wind turbine system ($f = 0.2$ to 0.4 Hz in the prototype scale).
- The hysteresis damping ratio of the horizontal force–displacement curve at the mudline is around 20% when the displacement amplitude normalised by the pile diameter at the mudline falls in the range of 1.5% to 5.0% for dense sand. A similar value is obtained for the moment-rotation curve at the mudline, but the value for the slender pile ($L/D = 8$) is around 10%. If attention is paid only to the cases with slow loading ($f = 0.002$ Hz), the slenderness-ratio dependency of the damping ratio can clearly be seen, and the smaller the slenderness ratio, the larger the hysteresis damping ratio, especially for the moment-rotation curve.
- With the fast cyclic loadings ($f = 0.2$ & 0.4 Hz), the build-up of excess pore water pressure is observed even in the dense sand, and the values are more or less the same throughout the depth irrespective of the imposed displacement amplitude. Even for the cyclic loading with the maximum horizontal displacement of 5% of the pile diameter, the state of the soil is far from being liquefied and the maximum value of the average excess pore water pressure ratio is around 50% in dense sand within the scope of this study.
- The bending moment profiles at the peaks of the load–displacement curves are very similar to those of the rigid pile in Gibson soil, even for the cases with the build-up of excess pore water pressure. Thus, the solution based on this, considering the soil resistance at the base, is used for a comparison with the observation in order to quantify the soil resistance at the base and the degradation of the soil resistance with cyclic loading.
- When the slenderness ratio of $L/D = 3.75$, i.e., the slenderness ratio is less than 5, the significant contribution of the moment resistance at the base is confirmed. If it is assumed that the monopile base acts as a rigid foundation on the Winkler foundation, assigning a vertical subgrade reaction modulus four times the horizontal one, which corresponds to vertical stiffness 1.5 times the horizontal one in a continuum halfspace, the experimental results can be reasonably explained within the scope of this study. It should also be noted that, with or without consideration given to the moment resistance at the base, the horizontal displacement at the mudline can change by 13% under the same applied load in this model.
- The minimum coefficient of the horizontal subgrade reaction, normalised by the coefficient in the first cycle, and the average excess pore water pressure ratio in the foundation ground show a one-to-one relationship. This suggests that, if the average pore water pressure ratio for the foundation ground and the resistance in the first loading can be estimated, it is possible to estimate the soil stiffness degradation for the steady-state.
- A comparison between the soil stiffness estimated by the pile loading tests and that by the undrained cyclic torsional shear tests on hollow cylindrical specimens reveals that their trends in stiffness decay with shearing are very similar. This suggests that, through cyclic shear tests for the determination of the deformation properties of soil in a laboratory, it is possible to estimate the degradation of the soil stiffness and parameters for the reduced sway-rocking type of foundation model.

Acknowledgements

The authors are grateful to Kawasaki Geological Engineering Company for their excellent work on soil testing and helpful discussions. The authors are indebted to Mr Sakae Seki, a technician at the Tokyo Institute of Technology, for his continuous cooperation with the centrifuge experiments.

Appendix A. Derivation of horizontal displacement of pile $x(z)$

The situation illustrated in Fig. 14 is considered. By satisfying the equilibrium condition in the direction normal to the pile axis and the equilibrium of moments around a certain point in the pile, for instance, around the base of the pile, the horizontal displacement of the pile at a depth of z, $x(z)$, when the pile is subjected to horizontal force H at the mudline level, is derived first. Since $x(z)$ changes linearly with depth, $x(z) = \{x(L) - x(0)\}z/L + x(0)$. When the equilibrium condition in the direction normal to the pile axis is satisfied,

$$\int_0^L (n_h z)x(z)dz + H_b = \frac{n_h L^2}{6}x(0) + \frac{(1+3\alpha_s)n_h L^2}{3}x(L) = H. \tag{A1}$$

Similarly, when the equilibrium of the moments around a certain point in the pile, for instance, around the base of the pile, is satisfied,

$$\begin{aligned} &-\int_0^L (n_h z)x(z)(L-z)dz + HL \\ &= -\frac{n_h L^3}{12}x(0) - \frac{n_h L^3}{12}x(L) + HL = M_b \\ &= \alpha_r n_h L^3\{x(0) - x(L)\}. \end{aligned} \tag{A2}$$

By obtaining $x(0)$ and $x(L)$ using Eqns. (A1) and (A2), $x(z)$ by horizontal force H only can be obtained as

$$x(z)|_{M=0} = -\frac{24(1+3\alpha_s)H}{(1+36\alpha_r+6\alpha_s+72\alpha_r\alpha_s)n_h L^3}\left\{z - \frac{3(1+4\alpha_r+4\alpha_s)}{4(1+3\alpha_s)}L\right\}. \tag{A3}$$

Next, by satisfying the equilibrium condition in the direction normal to the pile axis and the equilibrium of the moments around a certain point in the pile, the horizontal displacement of the pile at a depth of z, $x(z)$, when the pile is subjected to the moment M at the mudline level, is derived. When the equilibrium condition in the direction normal to the pile axis is satisfied,

$$\frac{n_h L^2}{6}x(0) + \frac{(1+3\alpha_s)n_h L^2}{3}x(L) = 0. \tag{A4}$$

Similarly, when the equilibrium of the moments around the base of the pile is satisfied,

$$-\frac{n_h L^3}{12}x(0) - \frac{n_h L^3}{12}x(L) + M = \alpha_r n_h L^3\{x(0) - x(L)\}. \tag{A5}$$

By obtaining $x(0)$ and $x(L)$ using Eqns. (A4) and (A5), $x(z)$ by the moment M only can be obtained as

$$x(z)|_{H=0} = -\frac{36(1+2\alpha_s)M}{(1+36\alpha_r+6\alpha_s+72\alpha_r\alpha_s)n_h L^4}\left\{z - \frac{2(1+3\alpha_s)}{3(1+2\alpha_s)}L\right\}. \tag{A6}$$

By adding Eqns. (A3) and (A6), i.e., $x(z) = x(z)|_{M=0} + x(z)|_{H=0}$, Eqn. (3) is obtained.

Appendix B. Rigid pile solution for the uniform ground

The solution for a ground with a constant subgrade reaction modulus on the rigid pile subjected to the lateral load can be derived by considering the soil resistance at the base in a similar way to that for the Gibson soil. If it is assumed that the moment resistance at the base is expressed as $M_b = K_r\theta = (\alpha_r k_h D L^3)\theta$ and the shear resistance at the base is expressed as $H_b = K_s x(L) = (\alpha_s k_h D L)x(L)$, where $x(L)$ is the horizontal displacement at the base ($z = L$) and α_r and α_s are constants, the horizontal displacement of the pile at a depth of z, $x(z)$, when the pile is subjected to horizontal force H and moment M at the mudline level, can be expressed as

$$\begin{aligned} x(z) = &-\frac{6(1+2\alpha_s)H}{(1+12\alpha_r+4\alpha_s+12\alpha_r\alpha_s)k_h D L^2}\left\{z - \frac{2(1+3\alpha_r+3\alpha_s)}{3(1+2\alpha_s)}L\right\} \\ &-\frac{12(1+\alpha_s)M}{(1+12\alpha_r+4\alpha_s+12\alpha_r\alpha_s)k_h D L^3}\left\{z - \frac{1+2\alpha_s}{2(1+\alpha_s)}L\right\}. \end{aligned} \tag{B1}$$

By using this equation, the relationship between the forces acting at the mudline (H, M) and the displacement and rotation at the mudline (u, θ) can be obtained as follows:

$$\begin{aligned} \begin{pmatrix} H \\ M \end{pmatrix} &= \begin{bmatrix} K_L & K_{LR} \\ K_{RL} & K_R \end{bmatrix}\begin{pmatrix} u \\ \theta \end{pmatrix} \\ &= \begin{bmatrix} (1+\alpha_s)k_h D L & -\left(\frac{1}{2}+\alpha_s\right)k_h D L^2 \\ -\left(\frac{1}{2}+\alpha_s\right)k_h D L^2 & \left(\frac{1}{3}+\alpha_r+\alpha_s\right)k_h D L^3 \end{bmatrix}\begin{pmatrix} u \\ \theta \end{pmatrix}. \end{aligned} \tag{B2}$$

The horizontal soil reaction, $p(z)$, can be determined by $p(z) = k_h D x(z)$. By double integrating this with appropriate boundary conditions, the moment distribution can be obtained as follows:

$$\begin{aligned} M(z) = &HL\left\{\left(\frac{z}{L}\right) - \frac{2(1+3\alpha_r+3\alpha_s)}{1+12\alpha_r+4\alpha_s+12\alpha_r\alpha_s}\left(\frac{z}{L}\right)^2 + \frac{1+2\alpha_s}{1+12\alpha_r+4\alpha_s+12\alpha_r\alpha_s}\left(\frac{z}{L}\right)^3\right\} \\ &+ M\left\{1 - \frac{3(1+2\alpha_s)}{1+12\alpha_r+4\alpha_s+12\alpha_r\alpha_s}\left(\frac{z}{L}\right)^2 + \frac{2(1+\alpha_s)}{1+12\alpha_r+4\alpha_s+12\alpha_r\alpha_s}\left(\frac{z}{L}\right)^3\right\}. \end{aligned} \tag{B3}$$

If we assume that $k_v = R_k k_h(L) = R_k n_h L/D$, by introducing the ratio of the vertical subgrade reaction modulus to the horizontal one, R_k, α_r in the above solution is expressed as follows:

$$K_r = \alpha_r k_h D L^3 = \frac{\pi R_k k_h D^4}{64} = \frac{\pi}{64} R_k \left(\frac{D}{L}\right)^3 k_h D L^3 \alpha_r = \frac{\pi}{64} R_k \left(\frac{D}{L}\right)^3. \quad \text{(B4)}$$

The expression of α_r is the same here as that for the Gibson soil.

References

Abadie, C.N., Byrne, B.W., Houlsby, G.T., 2019. Rigid pile response to cyclic lateral loading: laboratory tests. Géotechnique 69 (10), 863–876. https://doi.org/10.1680/jgeot.16.P.325.

API (American Petroleum Institute). 2000. *Recommended Practice for Planning, Designing and Constructing Fixed Offshore Platforms—Working Stress Design*, RP 2A-WSD, 21st Ed., Washington, DC, USA.

Baek, S.H., Kim, J., Lee, S.H., Chung, C.K., 2017. Development of the cyclic p-y curve for a single pile in sandy soil. Mar. Georesour. Geotechnol. 36 (3), 351–359. https://doi.org/10.1080/1064119X.2017.1318986.

Barber, E.S., 1953. Discussion to Paper "Load tests on fixed and freehead piles" by S.M. Gleser. ASTM, STP 154, 96–99.

Bayat, M., Andersen, L.V., Ibsen, L.B., 2016. p-y-ẏ curves for dynamic analysis of offshore wind turbine monopile foundations. Soil Dyn. Earthquake Eng. 90, 38–51. https://doi.org/10.1016/j.soildyn.2016.08.015.

Bhushan, K., Lee, L.J., Grime, D.B., 1981. Lateral load tests on drilled piers in sand. In: O'Neill (Ed.), Drilled Piers and Caissons. American Society of Civil Engineers, New York, NY, USA, pp. 114–131.

Blaney, G.W., O'Neill, M.W., 1986. Measured lateral response of mass on single pile in clay. J. Geotech. Eng. 112 (4), 443–457. https://doi.org/10.1061/(ASCE)0733-9410(1986)112:4(443).

Burd, H.J., Taborda, D.M.G., Zdravković, L., Abadie, C.N., Byrne, B.W., Houlsby, G.T., Gavin, K.G., Igoe, D.J.P., Jardine, R.J., Martin, C.M., McAdam, R.A., Pedro, A.M.G., Potts, D.M., 2020. PISA design model for monopiles for offshore wind turbines: application to a marine sand. Géotechnique 70 (11), 1048–1066. https://doi.org/10.1680/jgeot.18.P.277.

Carter, J.P., Kulhawy, F.H., 1992. Analysis of laterally loaded shafts in rock. J. Geotech. Eng. 118 (6), 839–855. https://doi.org/10.1061/(ASCE)0733-9410(1992)118:6(839).

Choo, Y.W., Kim, D., Park, J.H., Kwak, K., Kim, J.H., Kim, D.S., 2014. Lateral response of large-diameter monopiles for offshore wind turbines from centrifuge model tests. Geotech. Test. J. 37 (1), 107–120. https://doi.org/10.1520/GTJ20130081.

Choo, Y.W., Kim, D., 2016. Experimental development of the p-y relationship for large-diameter offshore monopiles in sands: Centrifuge tests. J. Geotech. Geoenviron. Eng. 142 (1), 04015058. https://doi.org/10.1061/(ASCE)GT.1943-5606.0001373.

Davisson, M.T., 1970. Lateral load capacity of piles. Highway Res. Rec. 333, 104–112.

DNVGL-ST-0126, 2018. Support structures for wind turbines, DNV, Høvik, Norway.

DNVGL-RP-C212, 2019. Offshore soil mechanics and geotechnical engineering, DNV, Høvik, Norway.

Elson, W.K., 1984. Design of laterally-loaded piles, CIRIA Report 103, Construction Industry Research & Information Association, London, UK.

Erbrich, C.T., O'Neill, M.P., Clancy, P., Randolph, M.F., 2011. Axial and lateral pile design in carbonate soils. In: Gourvenec, White (Eds.), Frontiers in Offshore Geotechnics II. CRC Press, Boca Raton, Florida, pp. 125–154.

Hanley, S., 2021. Vestas unveils world's most powerful offshore wind turbine, CleanTechnica, https://cleantechnica.com/2021/02/12/vestas-unveils-worlds-most-powerful-offshore-wind-turbine/.

Hetenyi, M., 1946. Beams on elastic foundations. University of Michigan Press, Ann Arbor, USA.

Higgins, W., Vasquez, C., Basu, D., Griffiths, D.V.G., 2013. Elastic solutions for laterally loaded piles. J. Geotech. Geoenviron. Eng. 139 (7), 1096–1103. https://doi.org/10.1061/(ASCE)GT.1943-5606.0000828.

Houlsby, G.T., Cassidy, M.J., Einav, I., 2005. A generalised Winkler model for the behaviour of shallow foundations. Géotechnique 55 (6), 449–460. https://doi.org/10.1680/geot.2005.55.6.449.

Iai, S., Tobita, T., Nakahara, T., 2005. Generalised scaling relations for dynamic centrifuge tests. Géotechnique 55 (5), 355–362. https://doi.org/10.1680/geot.2005.55.5.355.

IRENA. 2019. Future of wind: Deployment, investment, technology, grid integration and socio-economic aspects. (A Global Energy Transformation paper), International Renewable Energy Agency, Abu Dhabi, UAE. https://www.irena.org/-/media/Files/IRENA/Agency/Publication/2019/Oct/IRENA_Future_of_wind_2019.pdf.

IRENA, 2021. Offshore renewables: An action agenda for deployment, International Renewable Energy Agency, Abu Dhabi, UAE. https://www.irena.org/-/media/Files/IRENA/Agency/Publication/2021/Jul/IRENA_G20_Offshore_renewables_2021.pdf.

Kagawa, T., Kraft Jr., L.M., 1980. Lateral load-deflection relationships of piles subjected to dynamic loadings. Soils Found. 20 (4), 19–36. https://doi.org/10.3208/sandf1972.20.4_19.

Kamata, Y., Takahashi, A., 2021. Sway-rocking spring system applicable to short-rigid monopile foundations. Geotechnical and Geological Engineering 39 (4), 3065–3079. https://doi.org/10.1007/s10706-021-01678-2.

Lai, Y., Wang, L., Zhang, Y., Hong, Y.i., 2021. Site-specific soil reaction model for monopiles in soft clay based on laboratory element stress-strain curves. Ocean Eng. 220, 108437. https://doi.org/10.1016/j.oceaneng.2020.108437.

Leblanc, C., Houlsby, G.T., Byrne, B.W., 2010. Response of stiff piles in sand to long-term cyclic lateral loading. Géotechnique 60 (2), 79–90. https://doi.org/10.1680/geot.7.00196.

McAdam, R.A., Byrne, B.W., Houlsby, G.T., Beuckelaers, W.J.A.P., Burd, H.J., Gavin, K.G., Igoe, D.J.P., Jardine, R.J., Martin, C.M., Muir Wood, A., Potts, D.M., Skov Gretlund, J., Taborda, D.M.G., Zdravković, L., 2020. Monotonic laterally loaded pile testing in a dense marine sand at Dunkirk. Géotechnique 70 (11), 986–998. https://doi.org/10.1680/jgeot.18.PISA.004.

Nanda, S., Arthur, I., Sivakumar, V., Donohue, S., Bradshaw, A., Keltai, R., Gavin, K., Mackinnon, P., Rankin, B., Glynn, D., 2017. Monopiles subjected to uni- and multi-lateral cyclic loading. Geotech. Eng. 170 (3), 246–258. https://doi.org/10.1680/jgeen.16.00110.

Page, A.M., Grimstada, G., Eiksunda, G.R., Jostad, H.P., 2018. A macro-element pile foundation model for integrated analyses of monopile-based offshore wind turbines. Ocean Eng. 167, 23–35. https://doi.org/10.1016/j.oceaneng.2018.08.019.

Poulos, H.G., Davis, E.H., 1974. Elastic solutions for soil and rock mechanics. John Wiley and Sons, New York, USA.

Poulos, H.G., Davis, E.H., 1980. Pile Foundation Analysis and Design. John Wiley and Sons, New York, USA.

Rathod, D., Nigitha, D., Krishnanunni, K.T., 2021. Experimental Investigation of the Behavior of Monopile under Asymmetric Two-Way Cyclic Lateral Loads. Int. J. Geomech. 21 (3), 06021001. https://doi.org/10.1061/(ASCE)GM.1943-5622.0001920.

Richards, I.A., Bransby, M.F., Byrne, B.W., Gaudin, C., Houlsby, G.T., 2021. Effect of Stress Level on Response of Model Monopile to Cyclic Lateral Loading in Sand. J. Geotech. Geoenviron. Eng. 147 (3), 04021002. https://doi.org/10.1061/(ASCE)GT.1943-5606.0002447.

Scott, R.F., 1981. Foundation Analysis. Prentice-Hall, London, UK.

Shadlou, M., Bhattacharya, S., 2016. Dynamic stiffness of monopiles supporting offshore wind turbine generators. Soil Dyn. Earthquake Eng. 88, 15–32. https://doi.org/10.1016/j.soildyn.2016.04.002.

Taborda, D.M.G., Zdravković, L., Potts, D.M., Burd, H.J., Byrne, B.W., Gavin, K.G., Houlsby, G.T., Jardine, R.J., Liu, T., Martin, C.M., McAdam, R.A., 2020. Finite-element modelling of laterally loaded

piles in a dense marine sand at Dunkirk. Géotechnique 70 (11), 1014–1029. https://doi.org/10.1680/jgeot.18.P.277.

Takemura, J., Kondoh, M., Esaki, T., Kouda, M., Kusakabe, O., 1999. Centrifuge model tests on double propped wall excavation in soft clay. Soils Found. 39 (3), 75–87. https://doi.org/10.3208/sandf.39.3_75.

Terzaghi, K., 1955. Evaluation of coefficient of subgrade reaction. Géotechnique 5 (4), 297–326. https://doi.org/10.1680/geot.1955.5.4.297.

Xiao, S.H., Lin, K., Liu, H.J., Zhou, A.N., 2021. Performance analysis of monopile-supported wind turbines subjected to wind and operation loads. Renewable Energy 179, 842–858. https://doi.org/10.1016/j.renene.2021.07.055.

Zhang, L., 2009. Nonlinear analysis of laterally loaded rigid piles in cohesionless soil. Comput. Geotech. 36 (5), 718–724. https://doi.org/10.1016/j.compgeo.2008.12.001.

Zhang, Y., Andersen, K.H., 2017. Scaling of lateral pile p-y response in clay from laboratory stress-strain curves. Mar. struct. 53, 124–135. https://doi.org/10.1016/j.marstruc.2017.02.002.

Zhu, B., Li, T., Xiong, G., Liu, J.C., 2016. Centrifuge model tests on laterally loaded piles in sand. Int. J. Phys. Modell. Geotech. 16 (4), 160–172. https://doi.org/10.1680/jphmg.15.00023.

Zhu, B., Ren, J., Yuan, M., Zhu, J.S., Yang, Q.J., Gao, Y.F., Kong, D.Q., 2021. Centrifuge Modeling of Monotonic and Cyclic Lateral Behavior of Monopiles in Sand. J. Geotech. Geoenviron. Eng. 147 (8), 04021058. https://doi.org/10.1061/(ASCE)GT.1943-5606.0002566.